UNIVERSITY OF COPENHAGEN
FACULTY OF SCIENCE

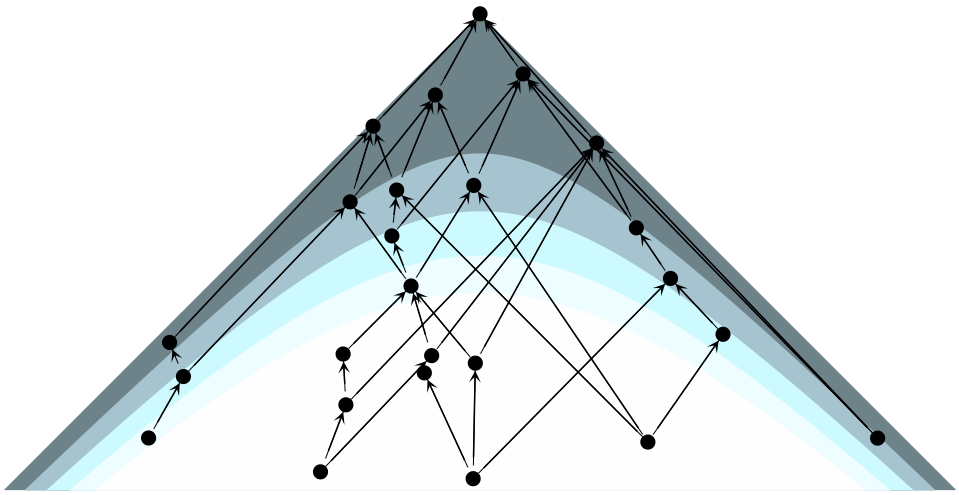

Master thesis

Higher curvature terms for Causal Sets

Extended proof and generalization for the Causal Set d'Alembertian

Christopher-Dustin Pfeiffer

Supervisor: Emil Bjerrum-Bohr
Co-Supervisor: Astrid Eichhorn

Submitted: May 20, 2022

Abstract

Causal Sets is a Quantum Gravity theory which postulates space-time to be emergent from partially ordered sets. These sets are causal in the sense that the order encodes the causality relations between the elements, which can be understood as space-time points. Einstein's theory of General Relativity describes gravity as curvature of space-time. This curvature is encoded in curvature operators like the Ricci-scalar R and the Ricci-tensor $R_{\mu\nu}$. To understand how a discrete causal set encodes the geometry of space-time and how space-time emerges from fundamental causal sets, it is important to be able to calculate curvature operators intrinsically from their causal order. It has already been shown that one can define an operator B, called Causal Set d'Alembertian, which acting on a causal set contains the Ricci-scalar in its continuum limit. This thesis presents an extended proof for the continuum limit of the Causal Set d'Alembertian in curved space-times of arbitrary dimension and finds a generalization of this operator that allows to extract higher orders of the Ricci-scalar R directly from the causal set. This new operator B^2 resembles a composition of the B-operator and contains both R^2 and $\Box R$ in its continuum limit. This limit is derived and both operators are assessed by numerical simulations on two-dimensional causal sets resembling Minkowski and de Sitter space-times.

Acknowledgments

I would like to thank my external supervisors Astrid Eichhorn and Gustavo de Brito from the Centre for Cosmology and Particle Physics Phenomenology (CP^3) at the University of Southern Denmark for the helpful discussions and their guidance throughout the project. I would also like to thank the entire research group for the good time I had there.

Contents

Chapter 1

Introduction

1.1 The problem of Quantum Gravity

Two of the most fundamental theories in physics today are Quantum Field Theory and General Relativity. Quantum Field Theory is concerned with quantum fields and their interactions. It is the language used to describe all the known fundamental particles, like for example electrons and quarks, and their interactions (except gravitation) in the standard model of particle physics. General Relativity is used to describe phenomena related to gravity. It depicts space-time as a Lorentzian manifold on which matter exists and describes the interaction between the manifold and the matter. Both theories have been very successful in their respective fields.

A fundamental difference between these two theories is that General Relativity is purely classical. At the moment there is no agreed upon way of quantizing General Relativity. This is already conceptually challenging as gravity in General Relativity is not described as a field on a space-time but as changes of space-time itself. The most straightforward way in analogy to other fundamental interactions is to quantize the space-time metric $g_{\mu\nu}$ around a fixed background metric and write for example $g_{\mu\nu} = \eta_{\mu\nu} + h_{\mu\nu}$, where here $\eta_{\mu\nu}$ is the metric of flat Minkowski space and $h_{\mu\nu}$ is the quantum field of gravity. When applying standard perturbative renormalization techniques on this setup it turns out that one needs an infinite number of counter terms to renormalize the theory. This is due to the Newton constant, which is the coupling constant for gravity, having mass-dimension -2 in natural units. The consequence is that there is an infinite number of parameters which need to be fixed by experiment. That makes the theory non-predictive and is the reason why gravity is said to be non-renormalizable.

A conservative approaches to tackle this problem is Asymptotic Safety [1], where non-perturbative renormalization techniques are used to try to find a ultraviolet (UV) fix point in the renormalization group flow, which would introduce relations between the

infinite number of terms in the Lagrangian and leave only a finite number of parameters to be fixed by experiment. Another possibility is to use canonical quantization in a background independent way, which leads to Loop Quantum Gravity and Spin Foams [2, 3]. Other approaches introduce more fundamental building blocks from which gravity emerges. The most popular example are strings in String Theory [4]. Of course there are many other approaches and proposals trying to tackle Quantum Gravity. One of them, Causal Sets, will be the outset for this thesis and is described in detail in the next section.

While trying to combine General Relativity and Quantum Mechanics, Quantum Gravity approaches also try to solve other problems particle physics and General Relativity currently face. For particle physics this includes the Laundau pole of the Standard Model, which means that the theory breaks down at some point when going to arbitrary high energies. In the case of General Relativity problems arise in the form of singularities in black holes and at the beginning of the universe where the theory is no longer applicable. These breakdowns of the theory are seen as an indication that a new description of physics is necessary. The singularities appear in regimes of high energy/small length scales where quantum fluctuations of the space-time metric are expected to play a role. Therefore it is expected that the singularities are just an artifact of the classical approximation and can be resolved, e.g. by a discrete spectrum of the corresponding quantum theory.

1.2 Introduction to Causal Sets

1.2.1 Motivation for Causal Sets

Customarily in General Relativity the metric encodes all the information on the causal relations of points in the space-time manifold (if they are space-, time- or light-like separated) and their distances to each other. The information on distances is related to information on scales and volume. Causal Sets, first proposed by Bombelli, Lee, Mayer and Sorkin in 1987 [5], is a quantum gravity theory which arose from the realization that conversely the causal order between points alone encodes almost all information about the metric. This statement has been made precise by various theorems. Some of the main ones can be found in [6–8]. Combined they can be summarized as [9]:

The causal structure of a past and future distinguishing space-time with dimension greater than 2 determines its dimension, topology, differentiable structure and metric up to a conformal factor.

Here past and future distinguishing means there are no causal (i.e. time-like or light-

like) loops in the space-time and no two different points have exactly the same causal past or future [10]. A conformal factor is a (generally position dependent) overall factor of the metric and related to information about the volume. Exactly this information about the size/volume of space-time regions is what is missing from the causal structure.

This problem can however be overcome if space-time is fundamentally discrete as then a notion of volume can be defined by simply counting the number of discrete points in a given region. In addition a fundamental discreteness could act as a natural cutoff and resolve the problems coming from UV divergences in Quantum Field Theory (e.g. the Landau pole) and curvature singularities in General Relativity. Another argument in favor of fundamental discreteness is that it makes the entanglement entropy of black holes finite [11, 12]. This is the entropy of a pure quantum state after tracing out the interior of the black hole and important as it is a possible explanation or part of the overall entropy of a black hole, which scales with the area of the horizon divided by the Planck-length squared.

The theorem also means that in contrast to other quantum gravity theories Causal Sets does not have to a priori assume a certain dimension or global hyperbolicity of the space-time and further also the Lorentzian nature, namely that there is exactly one time-like dimension, arises naturally from the causal order.

1.2.2 Kinematics of Causal Sets

The causal relation between points/elements of space-time can mathematically be described by a partial order. A partial order is a binary relation $\preceq$ between elements of a set that is anti-symmetric ($x \preceq y \wedge y \preceq x \Rightarrow x = y$) and transitive ($x \preceq y \wedge y \preceq z \Rightarrow x \preceq z$). Applied to causality anti-symmetric means that an event can not simultaneously be in the future and the past of another event, i.e. there are no causal loops, and transitivity means that if an event x happened in the past of y and y happened in the past of z then x also lies in the past light-cone of z. This leads us to the definition of a causal set [9]:

Def. *A causal set is defined as set $\mathcal{C}$ with an order relation $\preceq$ such that*

$$\forall x, y, z \in \mathcal{C} : x \preceq y \wedge y \preceq z \Rightarrow x \preceq z \tag{1.1a}$$

$$\forall x, y \in \mathcal{C} : x \preceq y \wedge y \preceq x \Rightarrow x = y \tag{1.1b}$$

$$\forall x, z \in \mathcal{C} : \textit{the set} \{y \mid x \preceq y \preceq z\} \textit{ is finite} \tag{1.1c}$$

In the definition of a causal set one finds again the definition of transitivity (1.1a) and anti-symmetry (1.1b), also known as non-circularity as it is related to the non-existence of

causal loops. The last condition is known as *local finiteness* and ensures the discreteness of the causal set.

As mentioned the discreteness in the causal set provides information about the volume by counting how many elements are in a given region of space-time. To ensure the number to volume correspondence, the elements must be uniformly distributed in the manifold we want to associate the causal set with. This uniform distribution is usually associated with a random *sprinkling* process, where the probability to have N elements in a space-time region of volume $\mathcal{V}$ is [13]

$$P(N) = \frac{(\rho\,\mathcal{V})^N\, e^{-\rho\,\mathcal{V}}}{N!}. \tag{1.2}$$

ρ is the fundamental density of the causal set. This *Poisson sprinkling* has the advantage that it provides the best number to volume correspondence for small volumes [14] and other than regular lattices or other triangulatians where each element only has a low number of neighbors, it does not induce a preferred frame in Minkowski space [15]. This makes causal sets fundamentally Lorentz invariant. This is in strong contrast to regular lattices, which after boost loose their uniformity as can be seen in figure 1.1 where both a causal set and a regular lattice are compared with a boosted version of themselves. In should be noted that in two dimensions one can build regular lattices that do not have this problem, but this is no longer possible in higher dimension [14].

A causal set $\mathcal{C}$ is then said to *embed faithfully* into a manifold $\mathcal{M}$ if there exists an embedding $f : \mathcal{C} \to \mathcal{M}$ such that 1) $f(x) \in J^-\left(f(y)\right)$ iff $x \prec y$, 2) the embedded points are distributed uniformly with density ρ, and 3) the continuous geometry varies only on a length scale much greater than the length scale of the causal set $l = \rho^{-\frac{1}{d}}$ [5, 16]. $J^-(\cdot)$ denotes the causal past and the first condition means that the order of the elements in the causal set is the same as the causal order of the points where the elements are embedded in the manifold. It is expected that if there exists a faithful embedding of a causal set into a manifold this manifold is essentially unique on scales greater than l. This is so far not proven in general and called the *Hauptvermutung* (engl: main conjecture) of causal sets. More precisely it states [5, 16]

Hauptvermutung. *If there exists $f_1 : \mathcal{C} \to (\mathcal{M}_1, g_1)$ and $f_2 : \mathcal{C} \to (\mathcal{M}_2, g_2)$ then $\mathcal{M}_1$ and $\mathcal{M}_2$ are related by a $\mathcal{C}$-preserving diffeomorphism $h : \mathcal{M}_1 \to \mathcal{M}_2$, where $\mathcal{C}$-preserving means $f_2 = h \circ f_1$, which is an approximate isometry of g_1 to g_2.*

Although the Hauptvermutung is not proven yet it is already clear that a lot of continuum information can be extracted from a causal set. This includes the dimension [17, 18] and

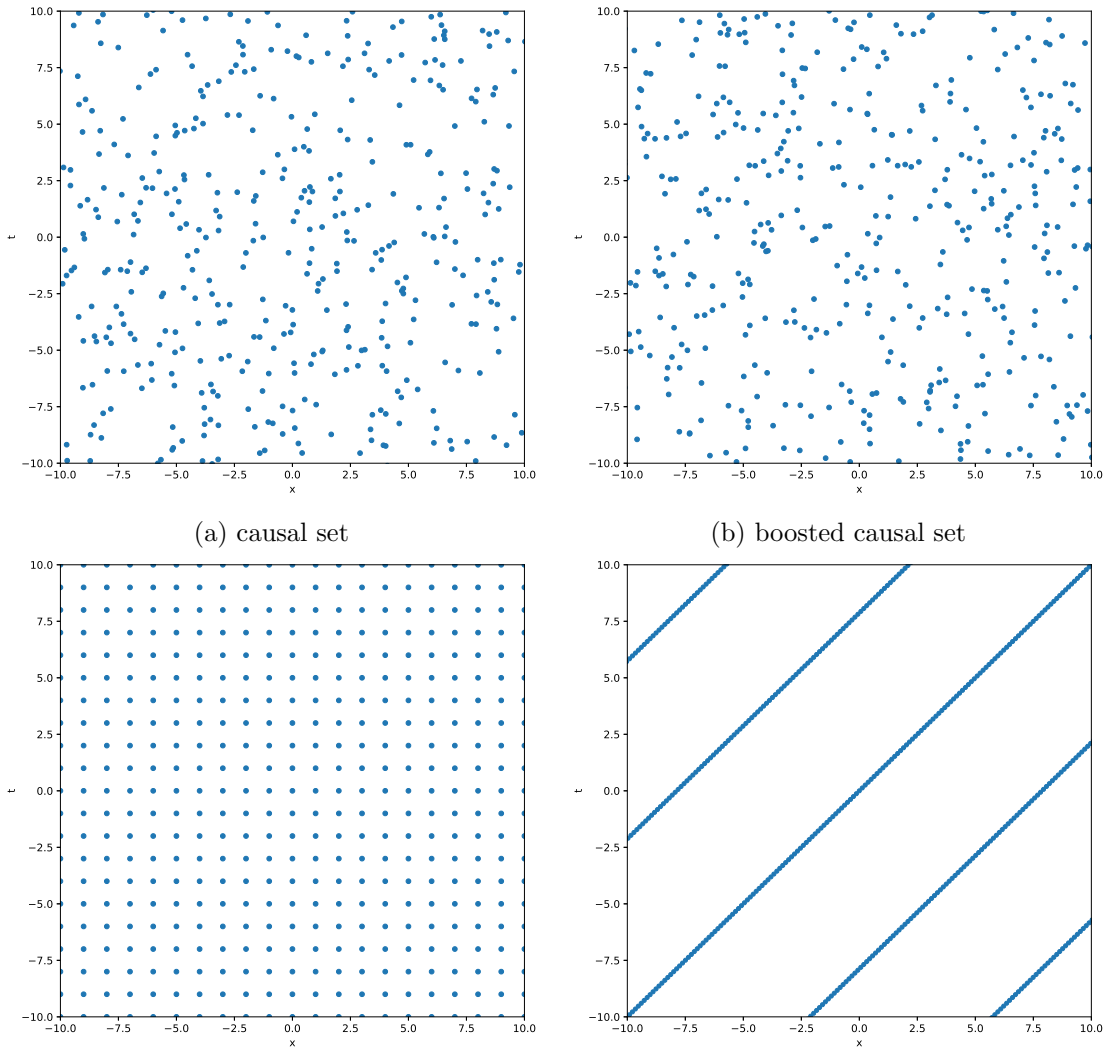

(a) causal set

(b) boosted causal set

(c) regular lattice

(d) boosted regular lattice

Fig. 1.1: a) part of a causal set sprinkled into a section of two-dimensional Minkowski space, b) the same section after the causal set was boosted with $\gamma = 4$;
c) a regular lattice in Minkowski space, d) points in regular lattice after a boost with $\gamma = 4$;
causal connections between elements are not shown

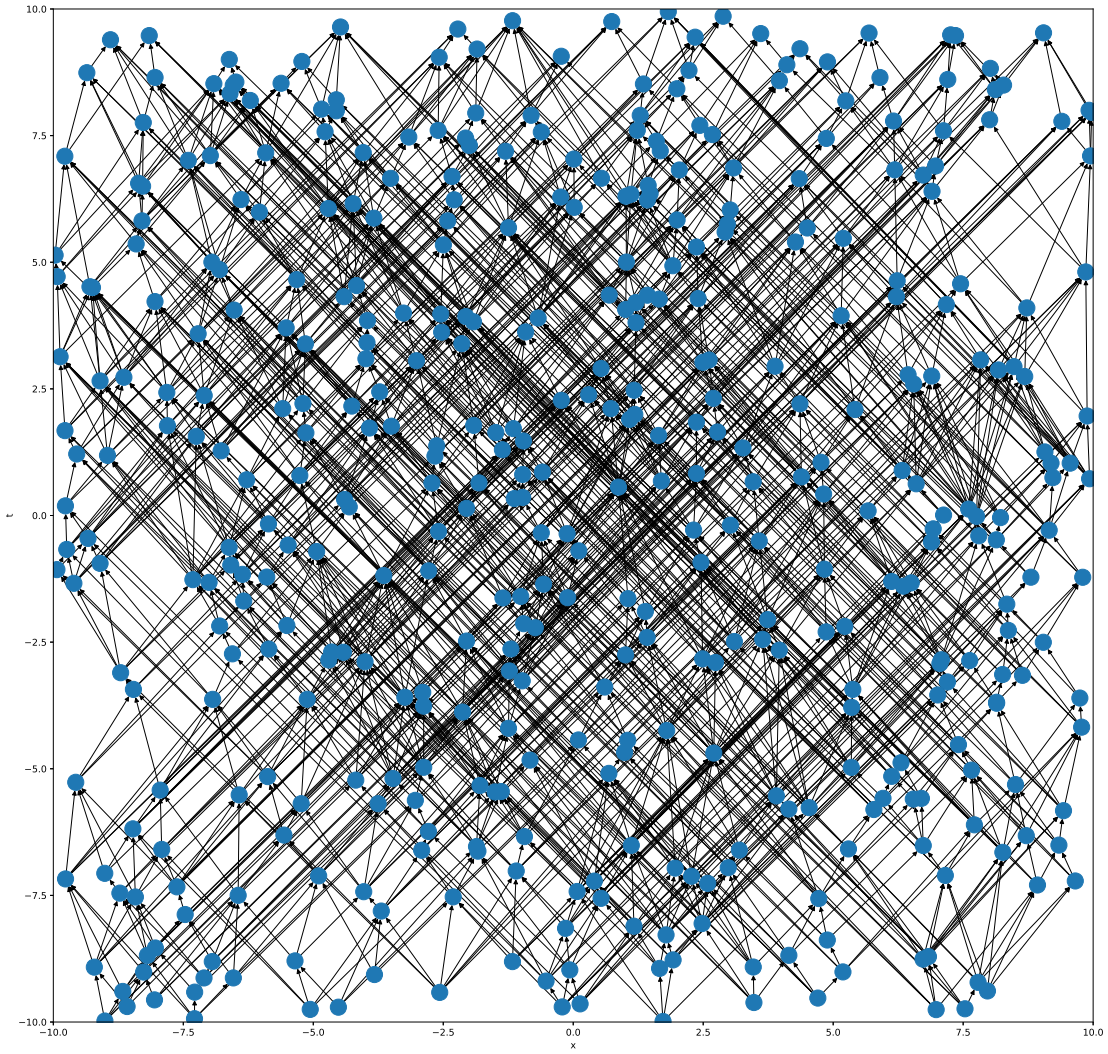

Fig. 1.2: Causal set with nearest neighbor connections between elements. Connections to elements outside the frame are not shown.

topology [19] of the manifold as well as time-like [20] and space-like [21] geodesic distances and scalar curvature [22].

Causal sets, just as any partially ordered set, can be visualized in a Hasse diagram. In a Hasse diagram only the relation to nearest neighbors are shown. Two elements x and y with $x \prec y$ are nearest neighbors iff there exists no element z such that $x \prec z \prec y$. ($x \prec y$ means $x \preceq y$ but $x \neq y$.) Elements which are higher in the order are shown further in the top and elements which precede them further to the bottom of the picture. For the causal set of figure 1.1c this is shown in figure 1.2. Here the causal set is also still embedded into two dimensional Minkowski space and one can see that the links between elements are mainly concentrated along the light cones. In many space-times a causal set element has in principle an infinite number of nearest neighbors in a narrow region along its light cone. This makes causal sets highly non-local.

1.2.3 Dynamics of Causal Sets

The dynamics of Causal Sets are still under development. The theory allows one to write the path integral over the metric as a sum over causal set configurations. The problem is that the sample space of such configurations is dominated by Kleitman-Rothschild type [23] and other non-manifold-like (i.e. not faithfully embeddable into a manifold) causal sets.

Causal sets of the Kleitman-Rothschild type for example consist of three layers with a quarter of the elements being in the first or third layer each and the rest being in the middle layer. In the causal set context, these would resemble space-times with only two time steps.

The challenge is therefore to find an action that suppresses the non-manifold like causal sets in the path sum. It has already been shown that the Benincasa-Dowker action [24], which is the causal set version of the Einstein-Hilbert action, can suppress two-level orders [25], which is another large class of non-manifold like causal sets.

Applications of the path sum over causal sets include Markov Chain Monte Carlo simulations on the set of two-dimensional causal sets. The simulations exhibit phase transitions between manifold-like and non-manifold-like causal sets, based on the value of a factor β which is introduced to turn the quantum measure $\exp\left(\frac{i}{\hbar}S(\mathcal{C})\right)$ into a probability measure $\exp\left(-\frac{\beta}{\hbar}S(\mathcal{C})\right)$ [26, 27]. In [28] the path sum over two-dimensional causal sets was used in a cosmological context.

Another, very different approach, which is however somewhat natural to causal sets and requires only a few basic assumptions are (classical) sequential growth models [29]. Here the causal set is "grown" by subsequent transitions in each of which an element

is added space-like or to the future of existing elements and each possible transition is given a probability.

The requirements imposed on the dynamics are *discrete general covariance* (the probability of transitioning from a causal set $\mathcal{C}$ to a causal set $\mathcal{C}'$ should not depend on the order in which elements are added), the *Bell causality condition* (the ratio of transition probabilities depends only on the elements in the past of the new element), and that the sum of probabilities of transition from a given causal set gives unity. An easy example is transitive percolation where the probability of the new element being in the future of another element is fixed. It was shown that in certain sequential growth models which exhibit a bouncing cosmology the dynamics converge towards transitive percolation [30].

One proceeds by defining a probability measure space for the causal sets. So far these growth models use classical probability distributions and the idea behind making classical sequential growth models quantum is to replace the classical probability measure with a quantum measure [31]. This can however in general not easily be extended to the whole sigma algebra (the collection of subsets closed under compliment and countable unions) [32], in which physically interesting configurations lie.

A more detailed review on Causal Sets can be found in [33].

1.3 Motivation

To be able to reconstruct continuum physics from a theory where causal sets are fundamental and to possibly proof the Hauptvermutung it is desirable within Causal Set Theory to be able to tell if a given causal set can be faithfully embedded into a manifold and reconstruct that manifold from the causal set if it is. Therefore it is important to find techniques that extract information about the manifold from a causal set. Several procedures to extract such information are already proposed in the literature [17–22] and this thesis aims to extend this list by providing a generalization of the Causal Set d'Alembertian, which allows for extracting higher powers of the Ricci-scalar directly from a causal set.

The Causal Set d'Alembertian $B^{(d)}(\cdot)$, defined in the next chapter, is an operator on causal sets that gives direct information about curvature in form of the Ricci-scalar R. It also appears in the Benincasa-Dowker action [24]

$$S_k^{(d)}(\mathcal{C}) = \hbar \frac{1}{\rho l_p^{d-2}} \sum_{x \in \mathcal{C}} B^{(d)}(-1), \tag{1.3}$$

where l_p in the formula is the Planck-length. It would be valuable to have more operators of this form. This would allow to extract more information about the curvature directly from the causal set and one could possibly construct more general terms for the action, that would correspond to terms beyond the Einstein-Hilbert action for General Relativity. With this one could study Causal Set dynamics in more variety and one could imagine to use causal sets in combination with alternative theories of gravity.

Motivation to extract information about higher order curvature from causal sets also comes from other Quantum Gravity theories, especially Asymptotic Safety. Stressing that physical discreteness in the dynamics and kinematical discreteness do not imply one another, causal sets can be seen as merely a UV regulator for the path integral over geometries [34]. The question then arises if the continuum limit for the dynamics of the regulator exists. The existence of a continuum limit is related to a fixed point when scaling the couplings of the theory. Finding such a fixed point would give an independent proof of the Asymptotic Safety conjecture, that gravity possesses an UV fixed point and is therefore renormalizable and predictive, in a Lorentzian setting. So far the Asymptotic Safety program uses mainly the Euclidean setting as the continuum techniques in a Lorentzian setting are technically challenging.

One way of finding such a fixed point is by refining the discretization while adjusting the coupling constants of the discrete theory in a way that keeps physical observables constant. If a continuum limit exists the coupling then flow towards the fixed point. The existence of a continuum limit and a fixed point then implies the existence of a second- or higher-order phase transition in the phase diagram of coupling constant space, where scale invariance can be enforced. [35] discusses this in the context of Causal Dynamical Triangulations [36], which is a way of discretizing space-time into spacial hypersurfaces which are triangulated by 4-simplices. The advantage of using causal sets instead, is the intrinsic Lorentzian nature of the theory, which does not rely on a foliation of space-time. Also taking the density of a causal set to infinity gives a clearer notion of a continuum limit then taking the length of lattice links in Causal Dynamical Triangulations to zero as the relation between the length of a lattice link has no clear correspondence to any physical length.

An alternative way to search for a continuum limit is to use the Renormalization Group equation for causal sets [34, 37] to look for a fixed point in the space of couplings. In both cases one first has to span the coupling space or rather a relevant sub-space thereof in which one wants to search for the fixed point. Calculations in the Euclidean setting indicate that the coupling of the R^2 term is relevant, i.e. a free parameter of the theory [38–40]. It would then be important to include the coupling associated with

this term in the search for a fixed point in the case of causal sets, which is why it is important to generalize the Causal Set d'Alembertian to higher orders and extend the Benincasa-Dowker action to include this term. Such an extension beyond Einstein-Hilbert is difficult to find for the action in Causal Dynamical Triangulations.

The rest of this thesis is structure as follows: In the next chapter the Causal Set d'Alembertian is defined and its continuum limit is proven for curved space-times of arbitrary dimension in chapter 3. Chapter 4 introduces a new operator which has R^2 and $\Box R$ in its continuum limit. Chapter 5 provides and introduction to numerical simulations for sprinkled causal sets and discusses simulation results for the Causal Set d'Alembertian and the new operator. At the end an outlook for the future of this research is presented.

Chapter 2

Introduction to the Causal Set d'Alembertian

After introducing causal sets as the foundation of space-time the question arises how matter fields propagate on this discrete background. The simplest form of a matter field is a scalar field ϕ. To describe its propagation one needs a causal set analog of the d'Alembertian operator $\Box = -\partial_t^2 + \partial_{x_1}^2 + \ldots + \partial_{x_d}^2$ ($c = 1$). Such an operator was first introduced in [13, 41] for two-dimensional causal sets, where it is defined as

$$B^{(2)}(\phi(x)) = 4\rho \left(-\frac{1}{2}\phi(x) + \sum_{y \in L_1(x)} \phi(y) - 2 \sum_{y \in L_2(x)} \phi(y) + \sum_{y \in L_3(x)} \phi(y) \right). \tag{2.1}$$

ρ is the density of the causal set and the sums run over contributions from different layers L_i. A layer is defined by

$$L_i(x) = \{ y \in \mathcal{C} \mid y \prec x \wedge |I(x,y)| = i + 1 \} \tag{2.2}$$

$$\text{with } I(x,y) = \{ z \in \mathcal{C} \mid y \preceq z \preceq x \}. \tag{2.3}$$

$I(x,y)$ is the causal interval between x and y. That is the intersection of the set of elements in the future of y with the set of elements in the past of x. Elements in $L_1(x)$ are exactly the nearest neighbors of x and an element $y \in L_i(x)$ has exactly $i+1$ elements (including x and y) in $I(x,y)$. Figure 2.1 visualizes this. It shows a causal set embedded into a cone in two dimensional Minkowski space. Elements in the first layer of the element at the tip of the cone are colored in red, elements in the second layer are colored in blue and elements in the third layer are colored orange. Other layers are not colored. The dashed lines indicate where the boundary between layers lies on average over many such causal sets.

The Causal Set d'Alembertian was extended to 4-dimensional causal sets [22, 24, 42]

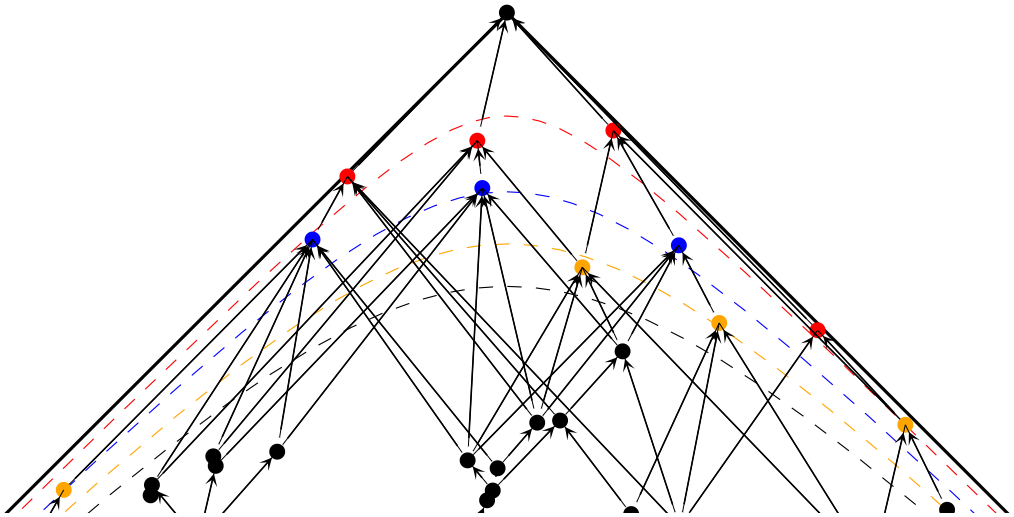

Fig. 2.1: Causal Set sprinkled into a cone in two dimensional Minkowski space. Elements in the first layer of the element at the tip of the cone are colored red, elements of the second layer are colored blue and elements of the third layer are colored orange. The expectation value for the boundary between layers are indicated by dashed lines.

by Benincasa and Dowker and later to the d-dimensional case [43, 44] by Dowker and Glaser. In d dimension the Causal Set d'Alembertian of a scalar field is defined as

$$B^{(d)}\left(\phi(x)\right) = \rho^{\frac{2}{d}} \left(\alpha_d \phi(x) + \beta_d \sum_{i=1}^{n_d} C_i^{(d)} \sum_{y \in L_i(x)} \phi(y) \right). \tag{2.4}$$

The constants α_d and β_d are dimension-dependent and have been found to be [44]

$$\alpha_d = \begin{cases} -2\frac{c_d^{\frac{2}{d}}}{\Gamma\left(\frac{d+2}{d}\right)} & \text{for even } d \\ -\frac{c_d^{\frac{2}{d}}}{\Gamma\left(\frac{d+2}{d}\right)} & \text{for odd } d \end{cases}, \qquad \beta_d = \begin{cases} \frac{2\Gamma\left(\frac{d}{2}+2\right)\Gamma\left(\frac{d}{2}+1\right)}{\Gamma\left(\frac{2}{d}\right)\Gamma(d)} c_d^{\frac{2}{d}} & \text{for even } d \\ \frac{d+1}{2^{d-1}\Gamma\left(\frac{2}{d}+1\right)} c_d^{\frac{2}{d}} & \text{for odd } d \end{cases} \tag{2.5}$$

$$\text{with } c_d = \frac{2\pi^{\frac{d-1}{2}}}{2^{\frac{d}{2}-1} d(d-1)\Gamma\left(\frac{d-1}{2}\right)}. \tag{2.6}$$

In (2.4) the first n_d layers are summed over and n_d is taken as $\left\lfloor \frac{d}{2} \right\rfloor + 2$ which is the minimum number necessary to achieve the right cancellations between the different layers. The definition of the $C_i^{(d)}$ will become clear shortly and an expression to compute them is given in [44].

In this form the Causal Set d'Alembertian at point x depends only on the past of x. Due to the nature of causal sets the operator is also non-local. It turns out that locality is restored in the continuum limit in the sense that the main contribution comes from an area close to x. We are interested the expectation value of the operator in the continuum limit. For this one first averages over all causal sets which could have originated from a sprinkling process. According to equation (1.2) the probability that a causal set element is sprinkled into a point y with infinitesimal Volume $\sqrt{-g}d^d y$ is $\rho\sqrt{-g}d^d y$ and the probability that this element at point y is in the i-th layer L_i relative to a causal set element sprinkled in point x, i.e. that there are $i-1$ elements in the causal interval between x and y, is $\frac{(\rho\,\mathcal{V}(x,y))^{i-1}}{(i-1)!} e^{-\rho\,\mathcal{V}(x,y)}$ where $\mathcal{V}(x,y)$ is the Volume of the causal interval between y and x. Therefore, when averaging over all sprinklings, summing over a layer becomes integrating all points in the causal past of x, $J^-(x)$, weighted with these probabilities:

$$\sum_{y \in L_i} \phi(y) \to \int_{J^-(x)} \phi(y) \frac{(\rho\,\mathcal{V}(x,y))^{i-1}}{(i-1)!} e^{-\rho\,\mathcal{V}(x,y)} \cdot \rho\sqrt{-g}d^d y. \tag{2.7}$$

Assuming there is a causal set element at point x, the Causal Set d'Alembertian (2.4)

then turns into the averaged Causal Set d'Alembertian

$$\begin{aligned}\bar{B}^{(d)}\left(\phi(x)\right) &= \mathbb{E}\left(B(\phi(x))\right) \\ &= \alpha_d \rho^{\frac{2}{d}} \phi(x) + \beta_d \rho^{\frac{d+2}{d}} \int_{J^-(x)} \sqrt{-g}\phi(y) \mathcal{P}_d(\rho\,\mathcal{V}) e^{-\rho\,\mathcal{V}(x,y)} d^d y,\end{aligned} \tag{2.8}$$

where

$$\mathcal{P}_d(\xi) e^{-\xi} = \sum_{i=1}^{n_d} C_i^{(d)} \frac{\xi^{i-1}}{(i-1)!} e^{-\xi} \tag{2.9}$$

is a dimension-dependent polynomial which can be written as

$$\mathcal{P}_d(\rho\,\mathcal{V}) e^{-\rho\,\mathcal{V}} = \mathcal{O}_d e^{-\rho\,\mathcal{V}}, \tag{2.10}$$

where

$$\mathcal{O}_{2n} = \frac{(d\rho\partial_\rho + 2)(d\rho\partial_\rho + 4)\ldots(d\rho\partial_\rho + 2n + 2)}{2^{n+1}(n+1)!} \text{ for even } d, \tag{2.11a}$$

$$\mathcal{O}_{2n+1} = \mathcal{O}_{2n} \text{ for odd } d. \tag{2.11b}$$

One can take this derivative operator together with (2.10) as the definition of the coefficients $C_i^{(d)}$ in the d'Alembertian.

As an example, in the two-dimensional case, one gets

$$\begin{aligned}&\bar{B}^{(2)}(\phi(x)) = \\ &\quad -2\rho\phi(x) + 4\rho^2 \int_{J^-(x)} \sqrt{-g}\phi(y) \left(1 - 2\rho\,\mathcal{V}(x,y) + \frac{1}{2}\left(\rho\,\mathcal{V}(x,y)\right)^2\right) e^{-\rho\,\mathcal{V}(x,y)} d^2 y.\end{aligned} \tag{2.12}$$

It turns out that when taking the limit $\rho \to \infty$ and as proven in chapter 3 one gets

$$\lim_{\rho\to\infty} \bar{B}(\phi(x)) = \Box\phi(x) - \frac{1}{2} R(x)\phi(x) \tag{2.13}$$

and the main contribution comes from a region close to x called W_1 in chapter 3.

Chapter 3

Proof for the limit of the Causal Set d'Alembertian in arbitrary space-times

3.1 Definitions and coordinates

Before looking into higher order curvature terms it is useful to review the derivation for the limit of the Causal Set d'Alembertian which gives the Ricci-scalar. Calculations to get R^2 will later involve the same kind of integrals and the results from this chapter can be used. The following derivation follows closely the general outline of [24, 42] but generalizes it to the n-dimensional case. It has already been shown in chapter 2 how the average over causal sets for the d'Alembertian is taken. The goal is now to show that

$$\begin{aligned} \bar{B}^{(d)}\left(\phi(x)\right) &= \alpha_d \rho^{\frac{2}{d}} \phi(x) + \beta_d \rho^{\frac{d+2}{d}} \int_{J^-(x)} \sqrt{-g}\phi(y)\mathcal{P}_d(\rho\,\mathcal{V}) e^{-\rho\,\mathcal{V}(x,y)} d^d y \\ &\xrightarrow[\rho\to\infty]{} \Box\phi(x) - \frac{1}{2}R(x)\phi(x). \end{aligned} \tag{3.1}$$

For this it has to be assumed that the field ϕ is at least two times differentiable at x and has compact support, so that the integration region becomes $J^-(x) \cap \operatorname{supp}\phi$ and is finite. $J^-(x)$ denotes the causal past of x. It will further be assume that ϕ does not diverge in the integration region. One can define Riemann normal coordinates [45] $\{y^\mu\}$ centered on x. In this coordinate system a point y has the coordinates $y^\mu = sa^\mu$ where s is the geodesic distance between x and y and a^μ is the unit tangent vector of this geodesic at x. The coordinates are locally flat and well defined as long as the geodesic from x to y is unique. In general dimension one can then define spatial polar coordinates $\{r, \theta_i\}$ in a neighborhood of x and the coordinates $u = \frac{1}{\sqrt{2}}\left(-y^0 - r\right)$ and $v = \frac{1}{\sqrt{2}}\left(-y^0 + r\right)$. Note that u and v are in this case defined to increase into the past which makes things easier since the integral will run over the causal past of x. One further defines Null Gaussian Normal Coordinates [46] $\{V, U, \theta_i\}$ in a neighborhood of $\partial J^-(x)$ that contains

$\partial J^-(x) \cap \operatorname{supp}\phi$. In this coordinate system V is the affine parameter along each null geodesic $\gamma(\{\theta_i\})$ emanating from x and $\{V, 0, \theta_i\}$ are coordinates of the light cone of which $\partial J^-(x)$ is the part in the past of x. U is defined as the affine parameter along the null geodesic at each point of the hypersurface $\{V, 0, \theta_i\}$ perpendicular to it. When also defined to be past directed, the Null Gaussian Normal Coordinates coincide with the Riemann Normal Coordinates in a region close to x where both coordinate systems are valid.

In the near region where the Riemann Normal Coordinates are valid the metric can be expanded as [43, 45]

$$g_{\mu\nu}(y) = \eta_{\mu\nu} - \frac{1}{3}R_{\mu\alpha\nu\beta}y^\alpha y^\beta + \dots \tag{3.2}$$

$$\sqrt{-g} = 1 - \frac{1}{6}R_{\mu\nu}y^\mu y^\nu + \dots \tag{3.3}$$

where the ellipsis stand for terms with higher order in curvature. The volume $\mathcal{V}(x,y)$ in the near region can be expanded in d dimensions as [33, 43, 47]

$$\mathcal{V}(x,y) = \mathcal{V}_{0d}\left(1 - \frac{d}{24(d+1)(d+2)}R\eta_{\mu\nu}y^\mu y^\nu + \frac{d}{24(d+1)}R_{\mu\nu}y^\mu y^\nu + O\left(R^2\right)\right), \tag{3.4}$$

$$\mathcal{V}_{0d} = 2\frac{\mathcal{V}\left(S_{d-2}\right)}{d(d-1)}\left(\frac{\tau}{2}\right)^d = c_d(uv)^{\frac{d}{2}}, \tag{3.5}$$

where $\mathcal{V}\left(S_{d-2}\right)$ is the volume of a S_{d-2} sphere and $\tau^2 = \eta_{\mu\nu}y^\mu y^\nu = 2uv$.

We can parallel transport a pseudo-orthonormal frame along each null geodesic emanating from x to define Null Fermi Normal Coordinates [48] $\{z^+, z^-, z^i\}$ at each point of a geodesic $\gamma(\{\theta_i\})$ such that a point y in the neighborhood of the geodesic with Gaussian Normal Coordinates $\{V, U, \theta_i\}$ lies at coordinates $\{z^+ = V, z^- = U, z^i = 0\}$. Following the prescription in [42], after an appropriate re-scaling of the Null Fermi Normal Coordinates the metric in the limit of small U becomes

$$ds^2 = U\left(-2dz^+dz^- + \delta_{ab}dz^a dz^b - R_{-a+b}\left(z^+\right)z^a z^b\left(dz^+\right)^2\right) + O\left(U^{\frac{3}{2}}\right) \tag{3.6}$$

and the Volume becomes

$$\mathcal{V}(x,y) = U^{\frac{d}{2}}f_0\left(V,\theta_i\right) + U^{\frac{d}{2}+1}f_1\left(U,V,\theta_i\right). \tag{3.7}$$

where $f_0(V,\theta_i)$ is an increasing function of V and is bigger than zero for positive V as the volume is zero for $V = 0$.

The integration region $J^-(x) \cap \operatorname{supp} \phi$ is divided into the three parts

$$W_1 = \left\{ y \in J^-(x) \mid 0 \leq u \leq v \leq a \right\}, \tag{3.8}$$

$$W_2 = \left\{ y \in J^-(x) \mid 0 \leq a' \leq V \leq L \wedge 0 \leq U \leq \frac{b^{\frac{2}{d}}}{f_0 \left(V, \theta_i\right)^{\frac{2}{d}}} \right\}, \tag{3.9}$$

$$W_3 = \left(J^-(x) \cap \operatorname{supp} \phi \right) \setminus \left(W_1 \cup W_2 \right). \tag{3.10}$$

W_1 is a small causal diamond to the past of x and W_2 is a region close to the light cone of x. W_3 are all other points in the support of ϕ and to the past of x. The parameter a is chosen small enough such that in W_1 the corrections to equations (3.3) and (3.4) are small and ϕ can be expanded as

$$\phi(y) = \phi(x) + \phi'(x)_\mu y^\mu + \frac{1}{2}\phi''(x)_{\mu\nu} y^\mu y^\nu + \psi(y) y^\mu y^\nu y^\sigma \tag{3.11}$$

with ψ being a function that captures all higher order terms. Accordingly b is chosen small enough such that for all $y \in W_2$ equation (3.7) is valid. L is chosen big enough and a' small enough so that $W_1 \cup W_2 \supseteq \partial J^-(x) \cap \operatorname{supp} \phi$ and that W_1 and W_2 overlap (so that there is no point in the integration region and near the light cone that is neither in W_1 nor in W_2).

3.2 The far region

First look at the region W_3. For all $y \in W_3$ the volume $\mathcal{V}(x, y)$ is bigger then zero and also $0 < \mathcal{V}_{\text{inf}} := \inf_{y \in W_3} \mathcal{V}(x, y)$. This is particularly because one can choose L to be finite since we have chosen ϕ to have compact support. Now one gets for the Integral

$$\left| \int_{W_3} d^d y \sqrt{-g} \phi(y) \mathcal{P}_d(\rho\, \mathcal{V}) e^{-\rho\, \mathcal{V}(x,y)} \right| \leq e^{-\rho\, \mathcal{V}_{\text{inf}}} \int_{W_3} d^d y \left| \sqrt{-g} \phi(y) \mathcal{P}_d(\rho\, \mathcal{V}) \right|. \tag{3.12}$$

This shows that this part of the integral declines exponentially with increasing ρ and will not contribute in the continuum limit.

3.3 The light cone region

Next look at the region W_2. The goal is to bound the absolute value of the integral over the region. One has

$$\left|\int_{W_2} d^d y\sqrt{-g}\phi(y)\mathcal{P}_d(\rho\,\mathcal{V})e^{-\rho\,\mathcal{V}_d(x,y)}\right| \tag{3.13}$$

$$= \left|\int_{a'}^{L} dV \int_{S^{d-2}} d\Omega \int_0^{\frac{b^{\frac{2}{d}}}{f_0(V,\theta_i)^{\frac{2}{d}}}} dU\sqrt{-g}\phi(y)\mathcal{O}_d e^{-\rho\,\mathcal{V}(x,y)}\right| \tag{3.14}$$

$$\leq \int_{a'}^{L} dV \int_{S^{d-2}} d\Omega \left|\mathcal{O}_d \int_0^{\frac{b^{\frac{2}{d}}}{f_0(V,\theta_i)^{\frac{2}{d}}}} dU\sqrt{-g}\phi(y)e^{-\rho\,\mathcal{V}(x,y)}\right| \tag{3.15}$$

$$= \int_{a'}^{L} dV \int_{S^{d-2}} d\Omega \left|\mathcal{O}_d \left|\int_0^{\frac{b^{\frac{2}{d}}}{f_0(V,\theta_i)^{\frac{2}{d}}}} dU\sqrt{-g}\phi(y)e^{-\rho\,\mathcal{V}(x,y)}\right|\right|. \tag{3.16}$$

For the last step the following identity was used.

$$\left|\frac{\partial}{\partial x}|f(x)|\right| = \left|\mathrm{sgn}\,(f(x))\,\frac{\partial}{\partial x}f(x)\right| = \left|\frac{\partial}{\partial x}f(x)\right| \tag{3.17}$$

Now, using the uniform norm on W_2 $\|f(y)\|_\infty = \sup_{y\in W_2}|f(y)|$ one can further bound the integral as

$$(3.16) \leq \int_{a'}^{L} dV \int_{S^{d-2}} d\Omega \left|\left\|\sqrt{-g}\right\|_\infty \|\phi\|_\infty \mathcal{O}_d \int_0^{\frac{b^{\frac{2}{d}}}{f_0(V,\theta_i)^{\frac{2}{d}}}} dU \left|e^{-\rho\,\mathcal{V}(x,y)}\right|\right| \tag{3.18}$$

$$= \left\|\sqrt{-g}\right\|_\infty \|\phi\|_\infty \int_{a'}^{L} dV \int_{S^{d-2}} d\Omega \left|\mathcal{O}_d \int_0^{\frac{b^{\frac{2}{d}}}{f_0(V,\theta_i)^{\frac{2}{d}}}} dU \left|e^{-\rho\,\mathcal{V}(x,y)}\right|\right|. \tag{3.19}$$

Everything in front of the integral is just a constant multiplying the rest and will be ignored in the following equations to make them shorter. Putting in equation (3.7) for

the volume and writing the second part of the exponential as a series yields

$$\int_{a'}^{L} dV \int_{S^{d-2}} d\Omega \left| \mathcal{O}_d \int_0^{\frac{b^{\frac{2}{d}}}{f_0(V,\theta_i)^{\frac{2}{d}}}} dU \left| e^{-\rho\left(U^{\frac{d}{2}} f_0(V,\theta_i) + U^{\frac{d}{2}+1} f_1(U,V,\theta_i)\right)} \right| \right| \tag{3.20}$$

$$= \int_{a'}^{L} dV \int_{S^{d-2}} d\Omega \left| \mathcal{O}_d \int_0^{\frac{b^{\frac{2}{d}}}{f_0(V,\theta_i)^{\frac{2}{d}}}} dU e^{-\rho U^{\frac{d}{2}} f_0(V,\theta_i)} \left| \sum_{l=0}^{\infty} \frac{(-1)^l \rho^l \left(U^{\frac{d}{2}+1}\right)^l}{l!} f_1(U,V,\theta_i)^l \right| \right|. \tag{3.21}$$

One can now get rid of the inner absolute value. As by using the triangle inequality and again the uniform norm on W_2 the integral can be bounded by

$$(3.21) \leq \int_{a'}^{L} dV \int_{S^{d-2}} d\Omega \left| \mathcal{O}_d \sum_{l=0}^{\infty} \frac{\|f_1(U,V,\theta_i)\|_\infty^l}{l!} \rho^l \int_0^{\frac{b^{\frac{2}{d}}}{f_0(V,\theta_i)^{\frac{2}{d}}}} dU\, U^{l\left(\frac{d}{2}+1\right)} e^{-\rho U^{\frac{d}{2}} f_0(V,\theta_i)} \right|. \tag{3.22}$$

From this the integral over U can be taken. When substituting $x = U^{\frac{d}{2}}$ that integral is of the form

$$\int_0^a dx\; x^{k-1} e^{-cx} = \frac{\gamma(k, ca)}{c^k} \quad (k > 0), \tag{3.23}$$

where $\gamma(k, m)$ is the lower incomplete gamma function. Defining $\lambda = l + \frac{2}{d}(l+1)$ one gets

$$(3.22) = \int_{a'}^{L} dV \int_{S^{d-2}} d\Omega \left| \mathcal{O}_d \sum_{l=0}^{\infty} \frac{\|f_1(U,V,\theta_i)\|_\infty^l}{l!} \rho^l \frac{2}{d} \int_0^{\frac{b}{f_0(V,\theta_i)}} dx\, x^{\lambda-1} e^{-\rho x f_0(V,\theta_i)} \right| \tag{3.24}$$

$$= \frac{2}{d} \int_{a'}^{L} dV \int_{S^{d-2}} d\Omega \left| \mathcal{O}_d \sum_{l=0}^{\infty} \frac{\|f_1(U,V,\theta_i)\|_\infty^l}{l!} \rho^l \frac{\gamma(\lambda, b\rho)}{\rho^\lambda f_0^\lambda(V,\theta_i)} \right|. \tag{3.25}$$

From here one can apply the triangle inequality again and then apply the operator $\mathcal{O}_d$. With $n = \lfloor \frac{d}{2} \rfloor$ such that $\mathcal{O}_d = \mathcal{O}_{2n}$ this results in

$$(3.25) \leq \frac{2}{d} \int_{a'}^{L} dV \int_{S^{d-2}} d\Omega \sum_{l=0}^{\infty} \frac{\|f_1(U,V,\theta_i)\|_\infty^l}{l! f_0^\lambda(V,\theta_i)} \left| \mathcal{O}_d \frac{\gamma(\lambda, b\rho)}{\rho^{\lambda-l}} \right| \tag{3.26}$$

$$= \frac{1}{2^n d(n+1)!} \int_{a'}^{L} dV \int_{S^{d-2}} d\Omega \sum_{l=0}^{\infty} \frac{\|f_1(U,V,\theta_i)\|_\infty^l}{l! f_0^\lambda(V,\theta_i)} \left| A_{\lambda,l}(n) \frac{\gamma(\lambda, b\rho)}{\rho^{\lambda-l}} + \sum_{k=0}^{n} (-1)^k B_{\lambda,l}(k+1,n) d^{1+k} b^{\lambda+k} \rho^{l+k} e^{-b\rho} \right|. \tag{3.27}$$

where for $n \geq 0$ and $0 \leq m \leq n+1$

$$A_{\lambda,l}(n) := \prod_{j=0}^{n} \left(d(l-\lambda) + 2j + 2 \right), \tag{3.28}$$

$$B_{\lambda,l}(m,n) := \begin{cases} A_{\lambda,l}(n), \text{if } m = 0 \\ 1, \text{if } m = n+1 \\ B_{\lambda,l}(m, n-1) \left(d(l+m-1) + 2n + 2 \right) + B_{\lambda,l}(m-1, n-1), \text{otherwise.} \end{cases} \tag{3.29}$$

The proof for this step is shown in appendix A. In equation (3.27) $f_0(V,\theta_i)$ is the only term left depending on the integration variables. By writing everything else in front of the integral and using the triangle inequality one last time, one can finally bound the original integral (3.13) by

$$\begin{aligned} &\left| \int_{W_2} d^d y \sqrt{-g} \phi(y) \mathcal{P}_d(\rho \mathcal{V}) e^{-\rho \mathcal{V}_d(x,y)} \right| \\ &\leq \frac{1}{2^n d(n+1)!} \left\| \sqrt{-g} \right\|_\infty \|\phi\|_\infty \cdot \\ &\sum_{l=0}^{\infty} \left[\frac{\|f_1(U,V,\theta_i)\|_\infty^l}{l!} \left(|A_{\lambda,l}(n)| \frac{\gamma(\lambda, b\rho)}{\rho^{\lambda-l}} + \sum_{k=0}^{n} |B_{\lambda,l}(k+1,n)| d^{1+k} b^{\lambda+k} \rho^{l+k} e^{-b\rho} \right) \right. \\ &\qquad \left. \cdot \int_{a'}^{L} dV \int_{S^{d-2}} d\Omega \frac{1}{f_0^\lambda(V,\theta_i)} \right]. \end{aligned} \tag{3.30}$$

Assuming $\sqrt{-g}$ does not diverge in W_2 and because $f_0(V,\theta_i) > 0$ for $V > 0$ everything in equ. (3.30) is finite and one can see that for $\rho \to \infty$ all terms either vanish exponentially

or are of the order $\rho^{l-\lambda} = \rho^{-\frac{2}{d}(l+1)}$. As in the d'Alembertian the integral is multiplied by a factor $\rho^{\frac{d+2}{d}}$ this means that in the d'Alembertian the region W_2 will contribute terms of order

$$\rho^{\frac{d+2}{d}} \rho^{-\frac{2}{d}(l+1)} = \rho^{1-l\frac{2}{d}}. \tag{3.31}$$

These terms will automatically vanish for $\rho \to \infty$ if $l > \frac{d}{2}$. For $l \leq \frac{d}{2}$ the terms are however zero anyways, because one has to take into account that they are all multiplied by $|A_{\lambda,l}(n)|$ and

$$A_{\lambda,l}(n) = \prod_{j=0}^{n} (d(l-\lambda) + 2j + 2) = \prod_{j=0}^{n} 2(j-l), \tag{3.32}$$

which is zero if $l \leq n \Leftrightarrow l \leq \lfloor \frac{d}{2} \rfloor$. This is equivalent with $l \leq \frac{d}{2}$ as l is an integer. From this one concludes that

$$\lim_{\rho \to 0} \int_{W_2} d^d y \sqrt{-g} \phi(y) \mathcal{P}_d(\rho \mathcal{V}) e^{-\rho \mathcal{V}_d(x,y)} = 0, \tag{3.33}$$

so that the region W_2 also does not contribute to the continuum limit. The region will however contribute corrections of order $\mathcal{O}\left(\rho^{-\frac{2}{d}}\right)$ for even dimension and $\mathcal{O}\left(\rho^{-\frac{1}{d}}\right)$ for odd dimension. The value of these corrections can unfortunately to current knowledge not be calculated in general space-times except one finds a way to express the functions $f_0(V, \theta_i)$ and $f_1(U, V, \theta_i)$ in the volume expansion in more detail.

3.4 The near region

3.4.1 Finding the contributing terms

For the region W_1 on can use the expansions (3.3), (3.4), and (3.11) as well as expanding the exponential and the integrals becomes

$$\begin{aligned}
&\int_{W_1} d^d y\sqrt{-g}\phi(y)\mathcal{P}_d(\rho\,\mathcal{V})e^{-\rho\,\mathcal{V}(x,y)} \\
&= \int_0^a dv \int_0^v du \int_{S^{d-2}} d\Omega \left(\frac{v-u}{\sqrt{2}}\right)^{d-2} \left(1-\frac{1}{6}R_{\mu\nu}(x)y^\mu y^\nu + T(y)y^\mu y^\nu y^\sigma\right) \\
&\qquad\qquad \left(\phi(x)+\phi'(x)_\mu y^\mu + \frac{1}{2}\phi''(x)_{\mu\nu}y^\mu y^\nu + \psi(y)y^\mu y^\nu y^\sigma\right) \\
&\qquad \mathcal{O}_d e^{-\rho c_d (uv)^{\frac{d}{2}}} \sum_{l=0}^{\infty} \frac{(-1)^l \rho^l c_d^l (uv)^{\frac{dl}{2}}}{l!} \left(-\frac{dR(x)\eta_{\mu\nu}y^\mu y^\nu}{24(d+1)(d+2)} + \frac{dR_{\mu\nu}(x)y^\mu y^\nu}{24(d+1)} + S(y)y^\mu y^\nu y^\sigma\right)^l
\end{aligned} \tag{3.34}$$

$T(y), \psi(y)$ and $S(y)$ are functions which capture all the higher order terms.

The goal now is to see which of these terms in the integral contribute to which order in ρ. After performing the angular integration one is left with terms of the form

$$\int_0^a dv \int_0^v du\,(v-u)^{d-2}\,(v-u)^\alpha (v+u)^\beta (uv)^{l\frac{d}{2}} \mathcal{O}_d \rho^l e^{-\rho c_d (uv)^{\frac{d}{2}}}. \tag{3.35}$$

Because everything inside the integral is radial symmetric one can change the integration limits in the following manner:

$$\int_0^a dv \int_0^v du \ldots \to \frac{1}{2}\int_0^a dv \int_0^a du \ldots \tag{3.36}$$

Also one has

$$(v-u)^{d-2+\alpha}\,(v+u)^\beta (uv)^{l\frac{d}{2}} \tag{3.37}$$

$$= \left[\sum_{i=0}^{\alpha+d-2} \binom{\alpha+d-2}{i} v^i (-u)^{\alpha+d-2-i}\right] \left[\sum_{j=0}^{\beta} \binom{\beta}{j} v^j u^{\beta-j}\right] (uv)^{l\frac{d}{2}} \tag{3.38}$$

$$= \sum_{i=0}^{\alpha+d-2} \sum_{j=0}^{\beta} \binom{\alpha+d-2}{i}\binom{\beta}{j} (-1)^{\alpha+d-2-i} v^{i+j+l\frac{d}{2}} u^{\alpha+\beta+d-2-i-j+l\frac{d}{2}}. \tag{3.39}$$

so that one is effectively left with a sum of integrals of the form

$$\int_0^a dv \int_0^a du\ v^{m+l\frac{d}{2}} u^{k+l\frac{d}{2}} \mathcal{O}_d e^{-\rho c_d (uv)^{\frac{d}{2}}} \tag{3.40}$$

and m, k are integers between 0 and $\alpha + \beta + d - 2$. It is important to note that

$$\max(m, k) \geq \left\lceil \frac{\alpha + \beta + d - 2}{2} \right\rceil. \tag{3.41}$$

To analyze the integral the first step is to perform a coordinate transformation $x = u^{\frac{d}{2}}, y = v^{\frac{d}{2}}$ to get

$$\frac{4}{d^2} \int_0^{\mathfrak{a}} dy \int_0^{\mathfrak{a}} dx\ y^{\mu} x^{\kappa} \mathcal{O}_d e^{-\rho c_d xy}, \tag{3.42}$$

where $\mathfrak{a} = a^{\frac{d}{2}}, \mu = \frac{2}{d}(m+1) + l - 1, \kappa = \frac{2}{d}(k+1) + l - 1$.

For the following it is assumed that $\mu \geq \kappa$. This can be done without loss of generality because the order of integration can be swapped. Then the solution of the integral is

$$\begin{aligned} \frac{4}{d^2} \frac{1}{2^{n+1}(n+1)!} \Bigg[& A_{\kappa+1,l}(n) \frac{\mathfrak{a}^{\mu+\kappa+2} \rho^l}{(\kappa+1)(\mu+1)}\ {}_2F_2 \left(\begin{matrix} \kappa+1, & \mu+1 \\ \kappa+2, & \mu+2 \end{matrix} \middle| -\mathfrak{a}^2 c_d \rho \right) \\ & + c_d^{-\mu-1} \mathfrak{a}^{\kappa-\mu} \rho^{l-\mu-1} \sum_{\iota=0}^{n} (-1)^{\iota} B_{\kappa+1,l}(\iota+1, n) d^{1+\iota} \gamma\left(\mu + \iota + 1, \mathfrak{a}^2 c \rho\right) \Bigg]. \end{aligned} \tag{3.43}$$

Here $n = \lfloor \frac{d}{2} \rfloor$ and $A_l(n), B_l(n, m)$ are defined as in the previous section or appendix A respectively. ${}_pF_q \left(\begin{matrix} a_1, \ldots, a_p \\ b_1, \ldots, b_q \end{matrix} \middle| z \right)$ is the generalized hypergeometric function. The details of the calculation can be found in Appendix B.

For the first term in (3.43) one can separate the two cases $\mu = \kappa$ and $\mu \neq \kappa$. For the case $\mu = \kappa$ it is useful to write the generalized hypergeometric function through the Meijer G-function [49]

$$\begin{aligned} {}_2F_2 \left(\begin{matrix} \kappa+1, & \mu+1 \\ \kappa+2, & \mu+2 \end{matrix} \middle| -\mathfrak{a}^2 c_d \rho \right) = \\ \frac{\Gamma(\kappa+2)\Gamma(\mu+2)}{\Gamma(\kappa+1)\Gamma(\mu+1)} G^{1,2}_{2,3} \left(\mathfrak{a}^2 c_d \rho \middle| \begin{matrix} \kappa, & \mu \\ 0, & \kappa-1, & \mu-1 \end{matrix} \right), \end{aligned} \tag{3.44}$$

as for $\mu = \kappa$ this can be further simplified by [50]

$$G^{1,2}_{2,3}\left(\mathfrak{a}^2 c_d \rho \,\middle|\, \begin{matrix} & \kappa, & \mu \\ 0, & \kappa-1, & \mu-1 \end{matrix}\right) = e^{-\mathfrak{a}^2 c_d \rho}\left(\mathfrak{a}^2 c_d \rho + \left(\mathfrak{a}^2 c_d \rho\right)^2\right). \tag{3.45}$$

So in the limit $\rho \to \infty$ the fist term in equ. (3.43) vanishes exponentially for $\mu = \kappa$.

For the case $\mu \neq \kappa$ the first term in equ. (3.43) can be transformed by using [51] and [52] as

$$A_{\kappa+1,l}(n)\frac{\mathfrak{a}^{\mu+\kappa+2}\rho^l}{(\kappa+1)(\mu+1)}\,{}_2F_2\left(\begin{matrix}\kappa+1, & \mu+1\\ \kappa+2, & \mu+2\end{matrix}\,\middle|\, -\mathfrak{a}^2 c_d\rho\right) \tag{3.46}$$

$$= A_{\kappa+1,l}(n)\frac{\mathfrak{a}^{\mu+\kappa+2}\rho^l}{(\kappa+1)(\mu+1)}\frac{1}{\mu-\kappa}\left[(\mu+1)_1F_1\left(\begin{matrix}\kappa+1\\ \kappa+2\end{matrix}\,\middle|\, -\mathfrak{a}^2 c_d\rho\right) - (\kappa+1)_1F_1\left(\begin{matrix}\mu+1\\ \mu+2\end{matrix}\,\middle|\, -\mathfrak{a}^2 c_d\rho\right)\right] \tag{3.47}$$

$$= A_{\kappa+1,l}(n)\frac{\mathfrak{a}^{\mu+\kappa+2}\rho^l}{\mu-\kappa}\left[\left(\mathfrak{a}^2 c_d\rho\right)^{-\kappa-1}\gamma\left(\kappa+1,\mathfrak{a}^2 c_d\rho\right) - \left(\mathfrak{a}^2 c_d\rho\right)^{-\mu-1}\gamma\left(\mu+1,\mathfrak{a}^2 c_d\rho\right)\right] \tag{3.48}$$

$$= \frac{A_{\kappa+1,l}(n)}{\mu-\kappa}\left[\mathfrak{a}^{\mu-\kappa}c_d^{-\kappa-1}\rho^{l-\kappa-1}\gamma\left(\kappa+1,\mathfrak{a}^2 c_d\rho\right) - a^{\kappa-\mu}c_d^{-\mu-1}\rho^{l-\mu-1}\gamma\left(\mu+1,\mathfrak{a}^2 c_d\rho\right)\right]. \tag{3.49}$$

This contributes to the order $l-\kappa-1$ and $l-\mu-1$ in ρ. In order to contribute in the continuum limit this has to be bigger or equal to $-\frac{d+2}{d}$. So for a term to contribute it needs $l-\kappa-1 = l-\left(\frac{2}{d}(k+1)+l-1\right)-1 \geq -\frac{d+2}{2} \Leftrightarrow k \leq \frac{d}{2}$ or $m \leq \frac{d}{2}$ respectively. However,

$$A_{\kappa+1,l}(n) = \prod_{\zeta=0}^{n}\left(d\left(l-(\kappa+1)\right)+2\zeta+2\right) \tag{3.50}$$

$$= \prod_{\zeta=0}^{n}\left(d\left(l-(\frac{2}{d}(k+1)+l-1+1)\right)+2\zeta+2\right) \tag{3.51}$$

$$= \prod_{\zeta=0}^{n} 2\left(-k+\zeta\right), \tag{3.52}$$

so that $A_{\kappa+1,l} = 0$ for $k \leq n = \lfloor\frac{d}{2}\rfloor$. Because k is an integer the term with $\rho^{l-\kappa-1}$ will not contribute and only give corrections of order $\rho^{-\frac{2}{d}}$ for even dimensions respectively $\rho^{-\frac{1}{d}}$ for odd dimensions and lower.

One is left with contributions of order $l-\mu-1$ and the contributions from the second term of equ. (3.43) which are of the same order. As it was assumed that $\mu \geq k \Leftrightarrow m \geq k$ and with equation (3.41) it is clear that m is at least $\left\lceil \frac{\alpha+\beta+d-2}{2} \right\rceil$. The condition $m \leq \frac{d}{2}$ for a term to contribute in the limit can then be transformed into the condition that $\alpha+\beta \leq 2$. The order of the corrections is again $\rho^{-\frac{2}{d}}$ for even dimensions and $\rho^{-\frac{1}{d}}$ for odd dimensions.

When applying these restriction to the original integral (3.34) only terms with at most order 2 in the coordinate y^μ fulfill them and one is left with only the three terms

$$\int_{W_1} d^d y \ \left(\phi(x) + \phi'(x)_\mu y^\mu + \frac{1}{2}\phi''(x)_{\mu\nu} y^\mu y^\nu\right) \mathcal{O}_d e^{-\rho c_d (uv)^{\frac{d}{2}}}, \tag{3.53}$$

$$\int_{W_1} d^d y \ \left(-\frac{1}{6} R_{\mu\nu}(x) y^\mu y^\nu\right) \phi(x) \mathcal{O}_d e^{-\rho c_d (uv)^{\frac{d}{2}}}, \tag{3.54}$$

$$\int_{W_1} d^d y \ \phi(x) \mathcal{O}_d \left(-\rho c_d (uv)^{\frac{d}{2}} \left(-\frac{dR(x)\eta_{\mu\nu} y^\mu y^\nu}{24(d+1)(d+2)} + \frac{dR_{\mu\nu}(x) y^\mu y^\nu}{24(d+1)}\right)\right) e^{-\rho c_d (uv)^{\frac{d}{2}}}. \tag{3.55}$$

3.4.2 Results for the remaining integrals

Remember that the averaged Causal Set d'Alembertian is

$$\bar{B}^{(d)}\left(\phi(x)\right) = \alpha_d \rho^{\frac{2}{d}} + \beta_d \rho^{\frac{d+2}{d}} \int_{J^-(x)} \sqrt{-g}\phi(y) \mathcal{O}_d e^{-\rho \mathcal{V}_d(x,y)} d^d y \tag{3.56}$$

and the goal was to show that

$$\lim_{\rho\to\infty} \bar{B}^{(d)}\left(\phi(x)\right) = \Box\phi(x) - \frac{1}{2} R(x)\phi(x). \tag{3.57}$$

From the three contributing terms of the integral (3.53) will give the contributions for $\Box\phi(x)$, and as shown in [44] (3.54) and (3.55) will result in $-\frac{1}{2}R(x)\phi(x)$ in the continuum limit. This section will focus on (3.53) and add some detail on how the results arise.

The first term of (3.53) will give rise to the integral

$$\mathcal{V}\left(S_{d-2}\right) \int_0^a dv \int_0^v du \left(\frac{v-u}{\sqrt{2}}\right)^{d-2} \phi(x) \mathcal{O}_d e^{-\rho c_d (uv)^{\frac{d}{2}}}. \tag{3.58}$$

This will give a non-vanishing contribution, but the Causal Set d'Alembertian is designed in a way that this contribution gets canceled. In fact as is done in [44], α_d can be derived

from the definition

$$\alpha_d := -\beta_d \lim_{\rho\to\infty} \rho\, \mathcal{V}\left(S_{d-2}\right) \int_0^a dv \int_0^v du \left(\frac{v-u}{\sqrt{2}}\right)^{d-2} \phi(x)\mathcal{O}_d e^{-\rho c_d (uv)^{\frac{d}{2}}}. \tag{3.59}$$

From this it is clear that the contribution of the first term in (3.53) will cancel with the first term of the d'Alembertian.

The second term in (3.53) will be proportional to

$$\int_0^a dv \int_0^v du (v-u)^{d-2}(v+u)\mathcal{O}_d e^{-\rho c_d (uv)^{\frac{d}{2}}} \tag{3.60}$$

after angular integration. This integral can be expanded as

$$\frac{1}{2}\sum_{i=0}^{d-2}\binom{d-2}{i}(-1)^{d-2-i}\int_0^a dv\int_0^a du\left(v^{i+1}u^{d-2-i}+v^i u^{d-2-i+1}\right)\mathcal{O}_d e^{-\rho c_d (uv)^{\frac{d}{2}}}. \tag{3.61}$$

In this step also the integration bounds where changed which is possible due to the fact that everything in the integral is radially symmetric. This allows one to later change the order of integration and effectively rename $v \to u, u \to v$. Using

$$\sum_{i=0}^{n}\binom{n}{i}x^i y^{n-i} = \sum_{i=0}^{n}\binom{n}{i}x^{n-i}y^i \tag{3.62}$$

the integral can be written as

$$\begin{aligned}\frac{1}{2}\sum_{i=0}^{d-2}\binom{d-2}{i}\Bigg[&(-1)^{d-2-i}\int_0^a dv\int_0^a du\; v^{i+1}u^{d-2-i}\mathcal{O}_d e^{-\rho c_d (uv)^{\frac{d}{2}}} \\ &+(-1)^i\int_0^a dv\int_0^a du\; v^{d-2-i}u^{i+1}\mathcal{O}_d e^{-\rho c_d (uv)^{\frac{d}{2}}}\Bigg].\end{aligned} \tag{3.63}$$

After renaming the variables and changing the order of integration in the second integral one finally gets

$$\frac{1}{2}\sum_{i=0}^{d-2}\binom{d-2}{i}\left[(-1)^{d-2-i}+(-1)^i\right]\int_0^a dv\int_0^a du\; v^{i+1}u^{d-2-i}\mathcal{O}_d e^{-\rho c_d (uv)^{\frac{d}{2}}}. \tag{3.64}$$

If d is odd all terms cancel and the result is 0. In even dimensions this cancellation does

not take place, but one has a sum of integrals of the form

$$\int_0^a dv \int_0^v du\ v^m u^k \mathcal{O}_d e^{-\rho c_d (uv)^{\frac{d}{2}}} \tag{3.65}$$

with

$$\min_i \max(m,k) = \frac{d}{2} + 1. \tag{3.66}$$

As was shown, in order to contribute to the continuum limit of the d'Alembertian a term must have $\max(m,k) \leq \frac{d}{2}$. Therefore this integral will not contribute to the continuum limit and only give corrections to it.

The last term in (3.53) contains $\Box\phi(x)$. By using $\Box\phi(x) = \left(-\partial_t^2 + \sum_i \partial_i^2\right)\phi(x)$ the integral after angular integration becomes

$$\frac{\mathcal{V}(S_{d-2})}{2} \int_0^a dv \int_0^v du \left(\frac{v-u}{\sqrt{2}}\right)^{d-2} \left[\frac{(v+u)^2}{2}\partial_t^2\phi(x) + \frac{(v-u)^2}{2(d-1)}\left(\partial_t^2 + \Box\right)\phi(x)\right] \mathcal{O}_d e^{-\rho c_d (uv)^{\frac{d}{2}}}. \tag{3.67}$$

Using the results from [44] one has for even dimensions

$$\lim_{\rho\to\infty} \beta_d \rho^{\frac{d+2}{d}} \frac{\mathcal{V}(S_{d-2})}{2} \int_0^a dv \int_0^v du \left(\frac{v-u}{\sqrt{2}}\right)^{d-2} \left(\frac{v+u}{\sqrt{2}}\right)^2 \mathcal{O}_d e^{-\rho c_d (uv)^{\frac{d}{2}}} \tag{3.68}$$

$$= \lim_{\rho\to\infty} \beta_d \rho^{\frac{d+2}{d}} \frac{\mathcal{V}(S_{d-2})}{2} \sum_{i=0}^{d-2}\sum_{j=0}^{2} \binom{d-2}{i}\binom{2}{j} \frac{(-1)^i}{2^{\frac{d}{2}}} \frac{a^{d+2}}{(i+j+1)(d+2)} \\ {}_{\frac{d}{2}+1}F_{\frac{d}{2}+1}\left(\begin{matrix}\frac{2}{d}(i+j+1), \frac{2}{d}+1, \ldots, 2 \\ \frac{2}{d}(i+j+1)+1, \frac{2}{d}, \ldots, 1\end{matrix}\middle| -a^d c_d \rho\right) \tag{3.69}$$

$$= -\beta_d \mathcal{V}(S_{d-2}) \frac{\Gamma\left(2+\frac{2}{d}\right)\Gamma(d-1)}{2^{\frac{d}{2}-1}(d+2)^2\Gamma\left(1+\frac{d}{2}\right)\Gamma\left(\frac{d}{2}\right)} = -1, \tag{3.70}$$

$$\lim_{\rho\to\infty}\beta_d\rho^{\frac{d+2}{d}}\frac{\mathcal{V}\left(S_{d-2}\right)}{2}\frac{1}{d-1}\int_0^a dv\int_0^v du\left(\frac{v-u}{\sqrt{2}}\right)^d\mathcal{O}_d e^{-\rho c_d(uv)^{\frac{d}{2}}} \tag{3.71}$$

$$=\lim_{\rho\to\infty}\beta_d\rho^{\frac{d+2}{d}}\frac{\mathcal{V}\left(S_{d-2}\right)}{2(d-1)}\sum_{i=0}^{d}\binom{d}{i}\frac{(-1)^i}{2^{\frac{d}{2}}}\frac{a^{d+2}}{(i+1)(d+2)} \\ {}_{\frac{d}{2}+1}F_{\frac{d}{2}+1}\left(\begin{matrix}\frac{2}{d}(i+1),\frac{2}{d}+1,\ldots,2\\ \frac{2}{d}(i+1)+1,\frac{2}{d},\ldots,1\end{matrix}\middle|\,-a^d c_d\rho\right) \tag{3.72}$$

$$=\beta_d\,\mathcal{V}\left(S_{d-2}\right)\frac{2^{\frac{d}{2}-1}\Gamma\left(\frac{2}{d}+1\right)\Gamma\left(\frac{d-1}{2}\right)}{d(d+2)\sqrt{\pi}\Gamma\left(\frac{d}{2}+1\right)c_d^{\frac{d+2}{d}}}=1, \tag{3.73}$$

and for odd dimensions

$$\lim_{\rho\to\infty}\beta_d\rho^{\frac{d+2}{d}}\frac{\mathcal{V}\left(S_{d-2}\right)}{2}\int_0^a dv\int_0^v du\left(\frac{v-u}{\sqrt{2}}\right)^{d-2}\left(\frac{v+u}{\sqrt{2}}\right)^2\mathcal{O}_d e^{-\rho c_d(uv)^{\frac{d}{2}}} \tag{3.74}$$

$$=\lim_{\rho\to\infty}\beta_d\rho^{\frac{d+2}{d}}\frac{\mathcal{V}\left(S_{d-2}\right)}{2}\sum_{i=0}^{d-2}\sum_{j=0}^{2}\binom{d-2}{i}\binom{2}{j}\frac{(-1)^i}{2^{\frac{d}{2}}}\frac{a^{d+2}}{(i+j+1)(d+2)} \\ {}_{\frac{d+1}{2}+2}F_{\frac{d+1}{2}+2}\left(\begin{matrix}1+\frac{2}{d},\frac{2}{d}(i+j+1),\frac{2}{d}+1,\ldots,2+\frac{1}{d}\\ 2+\frac{2}{d},\frac{2}{d}(i+j+1)+1,\frac{2}{d},\ldots,1+\frac{1}{d}\end{matrix}\middle|\,-a^d c_d\rho\right) \tag{3.75}$$

$$=-\beta_d\,\mathcal{V}\left(S_{d-2}\right)\frac{2^{\frac{d}{2}}\Gamma\left(\frac{2}{d}+1\right)}{d(d+1)(d-1)c_d^{\frac{d+2}{d}}}=-1, \tag{3.76}$$

$$\lim_{\rho\to\infty}\beta_d\rho^{\frac{d+2}{d}}\frac{\mathcal{V}\left(S_{d-2}\right)}{2}\frac{1}{d-1}\int_0^a dv\int_0^v du\left(\frac{v-u}{\sqrt{2}}\right)^d\mathcal{O}_d e^{-\rho c_d(uv)^{\frac{d}{2}}} \tag{3.77}$$

$$=\lim_{\rho\to\infty}\beta_d\rho^{\frac{d+2}{d}}\frac{\mathcal{V}\left(S_{d-2}\right)}{2(d-1)}\sum_{i=0}^{d}\binom{d}{i}\frac{(-1)^i}{2^{\frac{d}{2}}}\frac{a^{d+2}}{(i+1)(d+2)} \\ {}_{\frac{d+1}{2}+2}F_{\frac{d+1}{2}+2}\left(\begin{matrix}1+\frac{2}{d},\frac{2}{d}(i+1),\frac{2}{d}+1,\ldots,2+\frac{1}{d}\\ 2+\frac{2}{d},\frac{2}{d}(i+1)+1,\frac{2}{d},\ldots,1+\frac{1}{d}\end{matrix}\middle|\,-a^d c_d\rho\right) \tag{3.78}$$

$$=\beta_d\frac{\mathcal{V}\left(S_{d-2}\right)}{(d-1)}\frac{2^{\frac{d}{2}}\Gamma\left(\frac{2}{d}+1\right)}{d(d+1)c_d^{\frac{d+2}{d}}}=1. \tag{3.79}$$

So the final contribution is $\Box\phi(x)$.

To summarize, this chapter together with [44] shows that

$$\lim_{\rho\to\infty} \bar{B}^{(d)}\left(\phi(x)\right) = \Box\phi(x) - \frac{1}{2}R(x)\phi(x) \tag{3.80}$$

in any dimension $d \geq 2$. Further, it has also been shown that the first order corrections are of order $\rho^{-\frac{2}{d}}$ for even and $\rho^{-\frac{1}{d}}$ for odd dimension.

Chapter 4

Getting higher powers of the Ricci-Scalar

An easy way to get the higher order of some curvature terms is by applying the Causal Set d'Alembertian twice. This allows to define

$$
\begin{aligned}
&B^2(\phi(x)) := B\left(B(\phi(x))\right) \\
&= \rho^{\frac{2}{d}} \left(\alpha_d B\left(\phi(x)\right) + \beta_d \sum_{i=1}^{n_d} C_i^{(d)} \sum_{y \in L_i(x)} B\left(\phi(y)\right) \right) && (4.1) \\
&= \rho^{\frac{2}{d}} \left(\alpha_d \left[\rho^{\frac{2}{d}} \left(\alpha_d \phi(x) + \beta_d \sum_{i=1}^{n_d} C_i^{(d)} \sum_{z \in L_i(x)} \phi(z) \right) \right] + \right. && (4.2) \\
&\qquad \left. \beta_d \sum_{i=1}^{n_d} C_i^{(d)} \sum_{y \in L_i(x)} \left[\rho^{\frac{2}{d}} \left(\alpha_d \phi(y) + \beta_d \sum_{i=1}^{n_d} C_i^{(d)} \sum_{z \in L_i(y)} \phi(z) \right) \right] \right) .
\end{aligned}
$$

By averaging over sprinklings and transforming the sums into integrals as discussed at in chapter 3 one gets

$$
\begin{aligned}
\bar{B}^2(\phi(x)) =& \alpha_d \rho^{\frac{2}{d}} \left[\alpha_d \rho^{\frac{2}{d}} \phi(x) + \beta_d \rho^{\frac{d+2}{d}} \int_{J^-(x)} \sqrt{-g} \phi(z) \mathcal{P}_d(\rho\,\mathcal{V}) e^{-\rho\,\mathcal{V}_d(y,z)} d^d z \right] && (4.3) \\
&+ \beta_d \rho^{\frac{d+2}{d}} \int_{J^-(x)} \sqrt{-g} \left[\alpha_d \rho^{\frac{2}{d}} \phi(y) + \right. \\
&\qquad \left. \beta_d \rho^{\frac{d+2}{d}} \int_{J^-(y)} \sqrt{-g} \phi(z) \mathcal{P}_d(\rho\,\mathcal{V}) e^{-\rho\,\mathcal{V}_d(y,z)} d^d z \right] \mathcal{P}_d(\rho\,\mathcal{V}) e^{-\rho\,\mathcal{V}_d(x,y)} d^d y .
\end{aligned}
$$

Now assuming the field ϕ is at least two time differentiable in the entire region $J^-(x)$ and has compact support, one can first solve the inner integral using the results from

the previous chapter to get

$$\bar{B}^2(\phi(x)) = \alpha_d \rho^{\frac{2}{d}} \left[\Box\phi(x) - \frac{1}{2}R(x)\phi(x) + \Omega_0(x)\right] \tag{4.4}$$
$$+ \beta_d \rho^{\frac{d+2}{d}} \int_{J^-(x)} \sqrt{-g} \left[\Box\phi(y) - \frac{1}{2}R(y)\phi(y) + \Omega_0(y)\right] \mathcal{P}_d(\rho\,\mathcal{V}) e^{-\rho\,\mathcal{V}_d(x,y)} d^d y.$$

Here Ω_0 is a function of order $O(\rho^\kappa)$ with $\kappa < 0$ which captures the corrections to the continuum limit. Now, by defining $\psi(x) = \Box\phi(x) - \frac{1}{2}R(x)\phi(x) + \Omega_0(x)$ and assuming that ψ is two times differentiable at x one can again use the results from the previous chapter to solve the integral. The assumptions means that ϕ has to be at least 4 times partially differentiable at x and R and Ω are at least two times differentiable at x. The result is

$$\bar{B}^2(\phi(x)) = \Box\left[\Box\phi - \frac{1}{2}R\phi + \Omega_0\right](x) - \frac{1}{2}R(x)\left[\Box\phi - \frac{1}{2}R\phi + \Omega_0\right](x) + \Omega_1(x) \tag{4.5a}$$
$$= \Box(\Box\phi)(x) - \frac{1}{2}\Box\left(R(x)\phi(x)\right) + \Box\Omega_0(x) \tag{4.5b}$$
$$- \frac{1}{2}R(x)\Box\phi(x) + \frac{1}{4}R^2(x)\phi(x) - \frac{1}{2}\Omega_0(x) + \Omega_1(x)$$
$$= \left(\Box - R(x)\right)\Box\phi(x) - \frac{1}{2}(\Box R)(x)\phi(x) - \partial_i R(x)\partial^i\phi(x) + \frac{1}{4}R^2(x)\phi(x) + O(\rho^\kappa). \tag{4.5c}$$

Ω_1 is again a function of order $O(\rho^\kappa), \kappa < 0$. The derivatives of Ω_0 are of the same order in ρ as Ω_0 itself, because Ω_0 does not explicitly depend on any coordinates. The order of the first order corrections for $B^2\left(\phi(x)\right)$ in ρ is the same as for $B\left(\phi(x)\right)$.

In the special case of $\phi = 4$ in a compact region one has

$$\lim_{\rho\to\infty} \bar{B}^2\left(\phi(x)\right) = R^2(x) - 2\Box R(x). \tag{4.6}$$

This shows that the Causal Set d'Alembertian can also be used to geht higher orders of R and its derivatives. The next step would be B^3 which would give terms with $\Box^3, R\Box^2, \Box R\Box, R^2\Box, \Box^2 R, R\Box R, \Box R^2$, and R^3 acting on ϕ.

Chapter 5

Simulations

5.1 Introduction

The sprinkling of causal sets gives a very clear prescription on how to generate different causal sets from a given manifold. This allows for a method of testing operators on causal sets. First different causal sets are sprinkled in a manifold where the continuum result is known and thereafter the causal set operator in question is applied to the causal sets and the average is taken.

There exist already a few programs that generate sprinklings of causal sets [53, 54]. For this thesis another program was developed which can be found on github [55]. It is written in python. This makes the program slower but easy to run on any operating system and easy to adjust for other people as python is a popular programming language [56]. The program can sprinkle causal sets in a space-time cylinder, a causal cone or a causal diamond in Minkowski, de Sitter or Anti-de Sitter space-time in arbitrary dimension $d \geq 2, d \in \mathbb{N}$. The different forms of the sprinkling region are characterized by a depth τ and a radius R which can both be freely chosen. Their definition is depicted

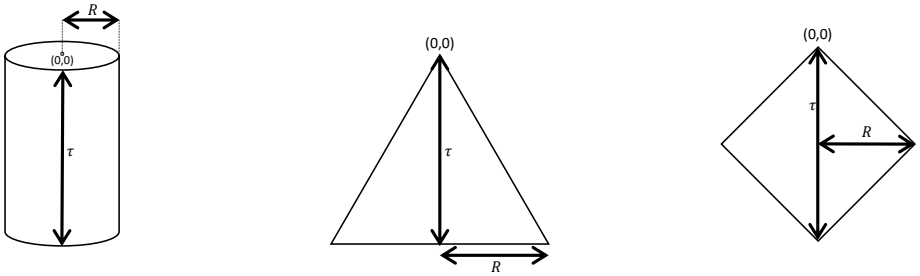

(a) cylinder (b) cone (c) diamond

Fig. 5.1: Different forms to sprinkle in.

in figure 5.1. The coordinates are chosen such that the origin is at the tip of the cone or diamond and in each sprinkling an element is added there. This element can later be used as point of evaluation for the operators B and B^2, which are also implemented. Other parameters for the sprinkling are the causal set density ρ as well as the curvature parameter l for de Sitter and Anti-de Siter space.

The sprinkling is generated by

1. sprinkling causal set elements
   a) sprinkling the time and radial coordinates in a cylinder
   b) removing unnecessary elements in case of cone or diamond
   c) sprinkling angular coordinates
2. connecting the elements
   a) connecting elements which are causal to each other and generate a directed graph
   b) performing transitive reduction, so that the graph only contains direct links (This step is not necessary for calculations of B and B^2, but the links encode all the relevant information about the causal set and might be relevant for other applications.)

Some details of the procedure are described in the next section.

5.2 Methodology

5.2.1 Sprinkling into d-dimensional Minkowski space

Sprinkling into Minkowski space can easily be done by choosing a random total number of elements from a Poisson distribution and then randomly distributing these points in a given space-time section in a way that preserves the volume to number relation. A very easy way to do this is to sprinkle into a space-time cylinder with height of proper time τ and whose spacial slices are described by a $(d-1)$-dimensional ball with radius R. Other forms of space-time regions like a causal diamond can then be obtained as a subset of the points in the cylinder by removing all the points that do not lie within them. The time coordinate can be drawn from a uniform distribution in the interval $[0, \tau]$ while the radius is first drawn from a power-distribution with density

$$P(r) = (d-1)r^{d-2}, \ r \in [0, 1] \tag{5.1}$$

and then multiplied by R to scale it to the target sphere size. In d dimensions one must further pick $d-2$ angles. The last angle ϕ can be picked from a uniform distribution on $[0, 2\pi]$ but for the other angles $\theta_i, i = 1, 2, ..., d-3$ one needs

$$P(\theta_i) = \frac{1}{\int_0^\pi \sin^i(x)dx} \sin^i(\theta), \ \theta \in [0, \pi]. \tag{5.2}$$

This is because how these angles contribute to the volume. For example in a three-dimensional ball there are more points with angle $\theta = \frac{\pi}{2}$ than $\theta = \frac{\pi}{4}$.

There exist multiple methods that allow to draw random numbers from a distribution given by a general probability density function $P(x)$ [57]. A first one to consider is the inversion method. For this, one needs the inverse of the cumulative distribution function $F(x)$ which in turn is the integral of the density function, i.e.

$$F(x) = \int_{-\infty}^{x} P(x')dx'. \tag{5.3}$$

Then random numbers with the desired distribution can be generated by generating random numbers u_i from a uniform distribution on $[0, 1]$ and calculating $x_i = F^-1(u_i)$.

As an example, see what that means if one wants to sprinkle a causal set into a cylinder in four-dimensional space-time. Each element has coordinates (t, r, θ, ϕ). t and ϕ can just be drawn from uniform distributions as described above. For r and θ the inversion method may be used. For the power-distribution this is often already implemented in packages for random number generation, therefore let's focus on how to draw random angles $\theta \in [0, \pi]$ from the probability density function $P(\theta) = \frac{1}{2}\sin(\theta)$. The corresponding cumulative distribution function is $F(\theta) = \frac{1}{2}(1 - \cos(\theta))$ and its inverse $F^-1(u) = \arccos(1 - 2u)$. To generate N random angles θ one now has to generate N uniformly distributed random numbers in the interval $[0, 1]$ and then calculate $F^-1(u)$ for each of them. This is indeed how it is implemented in the program for the four-dimensional case.

The inversion method has the advantage that it is straightforward and fast once the inverse cumulative distribution function is known. To sprinkle in a space-time with some arbitrary dimension d, however, this would necessitate to know the integral of $\sin^i(\theta)$ for $i = 1, ..., d-3$. Therefore, the program instead uses a simple version of rejection sampling to acquire random angles for dimensions greater than four. To draw a random angle from the probability distribution (5.2) first $\theta \in [0, \pi]$ is drawn from a uniform distribution together with y from a uniform distribution on $[0, 1]$. If $y \leq \sin^i(\theta)$ the angle is accepted and if $y > \sin^i(\theta)$ the angle is rejected and another attempt with new θ

and y is made. This will be repeated until the desired number of angles have successfully been drawn.

5.2.2 Sprinkling into de Sitter and Anti-de Sitter space

To test the Causal Set d'Alembertian B as well as B^2 one would also wish to be able to sprinkle into space-times with different curvature. For this the maximally symmetric space-times of de Sitter (dS) and Anti-de Sitter (AdS) space are an obvious choice. These can defined as hypersurfaces in a $(d+1)$-dimensional embedding space described by

$$\text{dS:} \ -X_0^2 + X_1^2 + X_2^2 + \cdots + X_d^2 = l_c^2, \tag{5.4}$$

$$\text{AdS:} \ -X_0^2 - X_1^2 + X_2^2 + \cdots + X_d^2 = -l_c^2 \tag{5.5}$$

and have the useful property that their line element can be written as

$$\text{dS: } ds^2 = -\frac{l_c^2 - r^2}{l_c^2}dt^2 + \frac{l_c^2}{l_c^2 - r^2}dr^2 + r^2 d\Omega^2, \tag{5.6}$$

$$\text{AdS: } ds^2 = -\frac{l_c^2 + r^2}{l_c^2}dt^2 + \frac{l_c^2}{l_c^2 + r^2}dr^2 + r^2 d\Omega^2. \tag{5.7}$$

with

de Sitter		Anti-de Sitter	
$X_0 = \sqrt{l_c^2 - r^2}\sinh\frac{t}{l_c}$	(5.8a)	$X_0 = \sqrt{l_c^2 + r^2}\sin\frac{t}{l_c}$	(5.9a)
$X_1 = \sqrt{l_c^2 - r^2}\cosh\frac{t}{l_c}$	(5.8b)	$X_1 = \sqrt{l_c^2 + r^2}\cos\frac{t}{l_c}$	(5.9b)
$X_i = r\Omega_{i-i}, \ i = 2, ..., d$	(5.8c)	$X_i = r\Omega_{i-i}, \ i = 2, ..., d$	(5.9c)

and the Ω_i defined as

$$\Omega_1 = \cos(\theta_1), \tag{5.10a}$$

$$\Omega_2 = \sin(\theta_1)\cos(\theta_2), \tag{5.10b}$$

$$\vdots \tag{5.10c}$$

$$\Omega_{d-2} = \sin(\theta_1)\ldots\sin(\theta_{d-2})\cos(\theta_{d-1}), \tag{5.10d}$$

$$\Omega_{d-1} = \sin(\theta_1)\ldots\sin(\theta_{d-2})\sin(\theta_{d-1}). \tag{5.10e}$$

If $d = 2$ then $X_2 = r$.

From (5.6) and (5.7) one can see that in these coordinates both de Sitter and Anti-de Sitter space have exactly the same volume element as Minkowski space in polar

coordinates. This has the huge advantage that one can sprinkle elements into a space-time cylinder just in the same way as one would do for Minkowski space and described in section 5.2.1. The difference between the three space-times arises in how these elements get connected in the causal set. While in Minkowski space the condition $\Delta s^2 \leq 0$ for two elements being causally connected simply becomes $\sum_{i=1}^{d} \Delta x^i \leq \Delta t$, where Δ stands for the difference in the coordinates, this is not as straightforward in de Sitter and Anti-de Sitter space-times. For this reason often conformal coordinates are used for sprinkling into de Sitter and Anti-de Sitter space instead [58]. There is however another simple way to calculate the geodesic distance in de Sitter space. For this, one has to calculate the coordinates $X(p)$ and $X(q)$ of the two points p and q in the $(d+1)$-dimensional space in which the de Sitter space is embedded in. From here, one calculates

$$Z(p,q) = l_c^{-2} X(p) \cdot X(q) \tag{5.11}$$

where the dot-product $X \cdot Y = -X_0 Y_0 + X_1 Y_1 + \cdots + X_d Y_d$ is defined through the metric of the embedding space. For Anti-de Sitter this will be $X \cdot Y = -X_0 Y_0 - X_1 Y_1 + X_2 Y_2 + \cdots + X_d Y_d$. The geodesic distance between p and q in de Sitter space is then simply [59, 60]

$$d(p,q) = l_c \operatorname{arccos} Z(p,q). \tag{5.12}$$

This can be adapted for Anti-de Sitter to

$$d(p,q) = l_c \operatorname{arccosh} Z(p,q). \tag{5.13}$$

To correctly link the causal set elements it is enough to know if they are time-like, null or space-like separated. For de Sitter p and q are causally connected (time-like or null separated) if $Z \geq 1$ and space-like if $Z < 1$. For Anti-de Sitter they are causally connected if $Z \leq 1$ and space-like if $Z > 1$.

Another useful relation is that the light cones emanating from a point with $r = 0, t = t_0$ are parameterized by

$$\text{dS: } r = l_c \tanh \frac{|t - t_0|}{l_c}, \tag{5.14}$$

$$\text{AdS: } r = l_c \tan \frac{|t - t_0|}{l_c}. \tag{5.15}$$

Therefore points with a given time-coordinate t and whose radial coordinate is smaller than given by these two equations are time-like to the point with $r = 0, t = t_0$. This leads

to easy conditions for elements being in a causal cone or causal diamond whose axis is the $r = 0$ line without having to calculate the coordinates in the embedding space. Sprinkling into a cone or diamond can then be done by sprinkling into a cylinder and removing all the elements that do not satisfy the conditions. The program uses the conditions resulting from equations (5.14) and (5.15) to eliminate the points outside the specified form already before assigning the angular coordinates and subsequently calculating the coordinates in the $(d+1)$-dimensional embedding space for the remaining elements.

5.2.3 Smearing

When trying to increase the number of elements in a given space-time volume to approach the continuum limit an important problem arises. Increasing the density ρ of the causal set also increases fluctuations of the Causal Set d'Alembertian over different sprinklings. For this reason Sorkin introduced the concept of smearing in [41]. The idea is that as one is mainly interested in the continuum limit of the operator averaged over many causal sets and tries to find a new operator with the same continuum limit but less fluctuations. When looking at the averaged Causal Set d'Alembertian (2.8) one can view ρ as just a parameter which is later taken to infinity in the continuum limit. Therefore one introduces another density ρ_k and replaces ρ with ρ_k to get

$$\bar{B}_k^{(d)}\left(\phi(x)\right) = \alpha_d \rho_k^{\frac{2}{d}} + \beta_d \rho_k^{\frac{d+2}{d}} \int_{J^-(x)} \sqrt{-g}\phi(y)\mathcal{O}_d^\star e^{-\rho_k \mathcal{V}(x,y)} d^d y. \tag{5.16}$$

$\mathcal{O}_d^\star$ is the same operator as $\mathcal{O}_d$ but with ρ_k replacing ρ everywhere. ρ_k is usually chosen smaller then ρ and introduces a new length scale $l_k = \rho_k^{-\frac{1}{d}} > l = \rho^{-\frac{1}{d}}$. The result is that the operator will be smeared. The meaning of "smeared" will become clearer at the end of this section.

In chapter 2 the averaged d'Alembertian (2.8) was obtained by averaging the Causal Set d'Alembertian (2.4) over sprinklings. Now the task is reverse. One wants to find an operator who has (5.16) as it's average over sprinklings. To get to the averaged d'Alembertian it was previously used that the probability of a causal set element being in the infinitesimal Volume $\sqrt{g}d^d y$ is $\rho\sqrt{-g}d^d y$ to turn the sum over elements into an integral. Now this step will be used in reverse. This relation between the form of the operator on a single causal set and it's average can be visualized as

$$\sum_{y \prec x} \cdots \leftrightarrow \rho \int_{J^-(x)} \sqrt{-g} \cdots d^d y. \tag{5.17}$$

Further, one uses that $\rho\,\mathcal{V}(x,y)$ is the expectation value of $N(x,y)$, the number of elements between x and y to replace $\mathcal{V}(x,y)$ by $\rho^{-1}N(x,y)$.

Applying these rules to get from the average (5.16) back to the operator on a single causal set on one gets

$$B_k^{(d)}\left(\phi(x)\right) = \alpha_d \rho_k^{\frac{2}{d}} + \beta_d \rho_k^{\frac{2}{d}} \frac{\rho_k}{\rho} \sum_{y \prec x} \phi(y) \mathcal{O}_d^\star e^{-\frac{\rho_k}{\rho} N(x,y)}. \tag{5.18}$$

The ratio $\frac{\rho_k}{\rho}$ is called ϵ. What is further done, since only the continuum limit of the operator has to be the same, is to view the exponential as the result of the limit

$$\lim_{N(x,y)\to\infty} \left(1 - \frac{\epsilon N(x,y)}{N(x,y)}\right)^{N(x,y)} = e^{-\epsilon N(x,y)} \tag{5.19}$$

and replacing it with $(1-\epsilon)^{N(x,y)}$ before applying $\mathcal{O}_d^\star$. For this reason it is important to start with $\mathcal{O}_d^\star$ appearing in (5.16) instead of $\mathcal{P}_d\left(\rho_k\,\mathcal{V}(x,y)\right)$ when doing the derivation in this direction.

Applying $\mathcal{O}_d^\star$ on $(1-\epsilon)^{N(x,y)}$ results in a similar structure as applying $\mathcal{O}_d$ on $e^{-\rho\,\mathcal{V}}$. The differences arise because the power N gets reduces by 1 after each differentiation. To see this, first look at $\mathcal{O}_{2n}^\star$ acting on $(1-\epsilon)^{N(x,y)}$ for $n = 1,\, 2$, i.e. for $2, 3$ or 4 dimensions:

$$\begin{aligned}
\mathcal{O}_2^\star\,(1-\epsilon)^N &= \frac{1}{8}(d\rho_k\partial_{\rho_k}+2)(d\rho_k\partial_{\rho_k}+4)\left(1-\frac{\rho_k}{\rho}\right)^N \qquad (5.20)\\
&= \frac{1}{8}\left[d^2\frac{\epsilon^2 N(N-1)}{(1-\epsilon)^2} - (d^2+6d)\frac{\epsilon N}{(1-\epsilon)} + 8\right](1-\epsilon)^N,\\
\mathcal{O}_4^\star\,(1-\epsilon)^N &= \frac{1}{48}(d\rho_k\partial_{\rho_k}+2)(d\rho_k\partial_{\rho_k}+4)(d\rho_k\partial_{\rho_k}+6)\,(1-\epsilon)^N \qquad (5.21)\\
&= \frac{1}{48}\left[-d^3\frac{\epsilon^3 N(N-1)(N-2)}{(1-\epsilon)^3} + (3d^3+12d^2)\frac{\epsilon^2 N(N-1)}{(1-\epsilon)^2}\right.\\
&\qquad \left. -(d^3+12d^2+44d)\frac{\epsilon N}{(1-\epsilon)} + 48\right](1-\epsilon)^N.
\end{aligned}$$

In these equations $N(x,y)$ is written as N for better readability. In comparison acting

with $\mathcal{O}_d$ on $e^{-\rho\,\mathcal{V}}$ yields

$$\begin{aligned}\mathcal{O}_2 e^{-\rho\,\mathcal{V}} &= \frac{1}{8}(d\rho\partial_\rho + 2)(d\rho\partial_\rho + 4)e^{-\rho\,\mathcal{V}} \qquad (5.22)\\ &= \frac{1}{8}\left[d^2\rho^2\,\mathcal{V}^2 - (d^2+6d)\rho\,\mathcal{V} + 8\right] e^{-\rho\,\mathcal{V}},\\ \mathcal{O}_4 e^{-\rho\,\mathcal{V}} &= \frac{1}{48}(d\rho\partial_\rho + 2)(d\rho\partial_\rho + 4)(d\rho\partial_\rho + 6)e^{-\rho\,\mathcal{V}} \qquad (5.23)\\ &= \frac{1}{48}\left[-d^3\rho^3\,\mathcal{V}^3 + (3d^3+12d^2)\rho^2\,\mathcal{V}^2\right.\\ &\qquad \left. -(d^3+12d^2+44d)\rho\,\mathcal{V} + 48\right] e^{-\rho\,\mathcal{V}}.\end{aligned}$$

Comparing equations (5.20), (5.21) with (5.22), (5.23) the pattern becomes clearer. By the definition of $C_i^{(d)}$ it is known that

$$\mathcal{O}_d e^{-\rho\,\mathcal{V}} = e^{-\rho\,\mathcal{V}} \sum_{i=1}^{n_d} C_i^{(d)} \frac{(\rho\,\mathcal{V})^{i-1}}{(i-1)!}. \qquad (5.24)$$

The conclusion here is that

$$f(N,\epsilon) := \mathcal{O}_d^\star (1-\epsilon)^N = (1-\epsilon)^N \left(C_1^{(d)} + \sum_{i=1}^{n_d-1} C_{i+1}^{(d)} \frac{\epsilon^i N(N-1)\dots(N-i+1)}{i!(1-\epsilon)^i} \right). \qquad (5.25)$$

Applying this to equation (5.18) one gets the new operator

$$B_k^{(d)}\left(\phi(x)\right) = \rho_k^{\frac{2}{d}} \left(\alpha_d \phi(x) + \beta_d \epsilon \sum_{y \prec x} f\left(N(x,y),\epsilon\right) \phi(y) \right). \qquad (5.26)$$

This new operator is actually a one parameter family of Causal Set d'Alembertians. The original Causal Set d'Alembertian is just the spacial case of $\epsilon \to 1$ or equivalently $\rho_k \to \rho$.

In the original Causal Set d'Alembertian one sums over the first n_d layers and weights each of them with $C_i^{(d)}$. In this "smeared" d'Alembertian one sums over every layer and gives it weight $\epsilon f(i-1,\epsilon)$. Figure 5.2 shows the weights for the layers in two dimensions for $\epsilon = 0.3$ and $\epsilon = 0.05$. In the un-smeared version the weights are 1 for layer 1, -2 for layer 2 and 1 for layer 3. In the smeared version the weights are "smeared" over a wider (infinite) range of layers. One can see that for stronger smearing/smaller ϵ the weights individual layers get are smaller, but the number of layers which give a significant contribution increases.

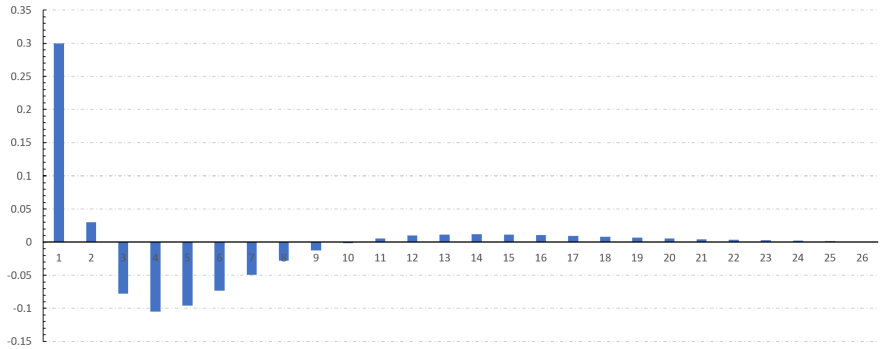

(a) $\epsilon = 0.3$

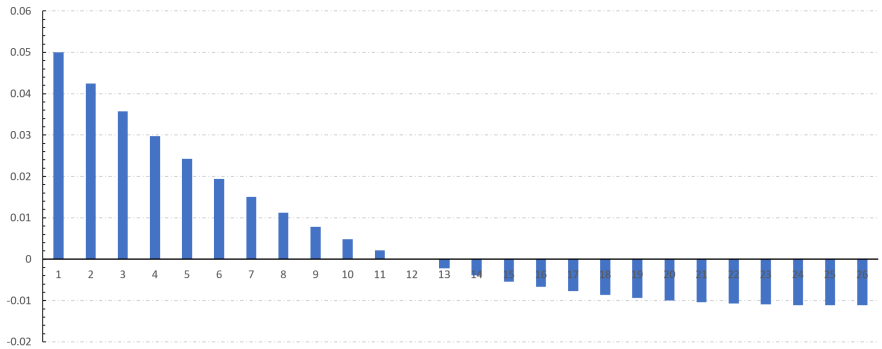

(b) $\epsilon = 0.05$

Fig. 5.2: Weighting for the first 26 layers in the smeared Causal Set d'Alembertian in two dimensions for $\epsilon = 0.3$ and $\epsilon = 0.05$.

When applying the same procedure to the $B^2(\phi)$ operator one gets

$$B_k^2(\phi) = (\epsilon_o \rho)^{\frac{2}{d}} \left(\alpha_d \left[(\epsilon_i \rho) \left(\phi(x) + \beta_d \epsilon_i \sum_{y \prec x} f\left(N(x,y), \epsilon_i\right) \phi(y) \right) \right] + \right. \tag{5.27}$$
$$\left. \beta_d \epsilon_o \sum_{y \prec x} f\left(N(x,y), \epsilon\right) \left[(\epsilon_i \rho) \left(\phi(y) + \beta_d \epsilon_i \sum_{z \prec y} f\left(N(y,z), \epsilon_i\right) \phi(z) \right) \right] \right).$$

ϵ_o describes the smearing of the outer B operator and ϵ_i the smearing of the inner B operator. If one views the necessity of smearing to get the fluctuations under control as a hint for the existence of a physical meso-scale l_k, as is often done in the literate one would expect $\epsilon_o = \epsilon_i$. If one however views smearing as a pure mathematical tool and additional parameter in defining the operator, they are a priori independent. The simulation program allows for them to be set independently.

5.3 Run-time behavior

This section is a short description on how the run-time of the simulation scales when increasing the number of causal set elements. In generating the causal set, connecting the elements, which is done by first looping through them and checking if they are causally related and then doing a transitive reduction on the resulting graph to only have the direct links left, takes the longest time. This procedure scales in the order $O(N^2)$, where N is the number of elements in the causal set. On a surface book 2 with Intel i7-8650U processor it takes about 0.3 seconds to sprinkle a causal set with $N = 600$ into a two-dimensional diamond in Minkowski space and about 2.2 seconds for $N = 1500$.

Calculating the value of the operators $B(\phi)$ and $B^2(\phi)$ on the causal set is really fast in the non-smeared version as only sums over the first few layers have to be performed. But in the smeared version the sum in B goes over the entire causal past of the starting point and for each element its layer needs to be found as this gives $N(x, y)$ which now enters into the formula. The calculation is therefore of the order $O(N^2)$. For B^2 at each node the operator B has to be calculated and the calculation scales in the order $O(N^3)$. For $N = 600$ it took around 0.2 seconds to calculate a value for B^2 with $\epsilon \neq 1$ and for $N = 1500$ around 3.3 seconds.

When running simulations one should make use of the fact, that generating causal sets and calculating the value of the operators on them can easily be parallelized.

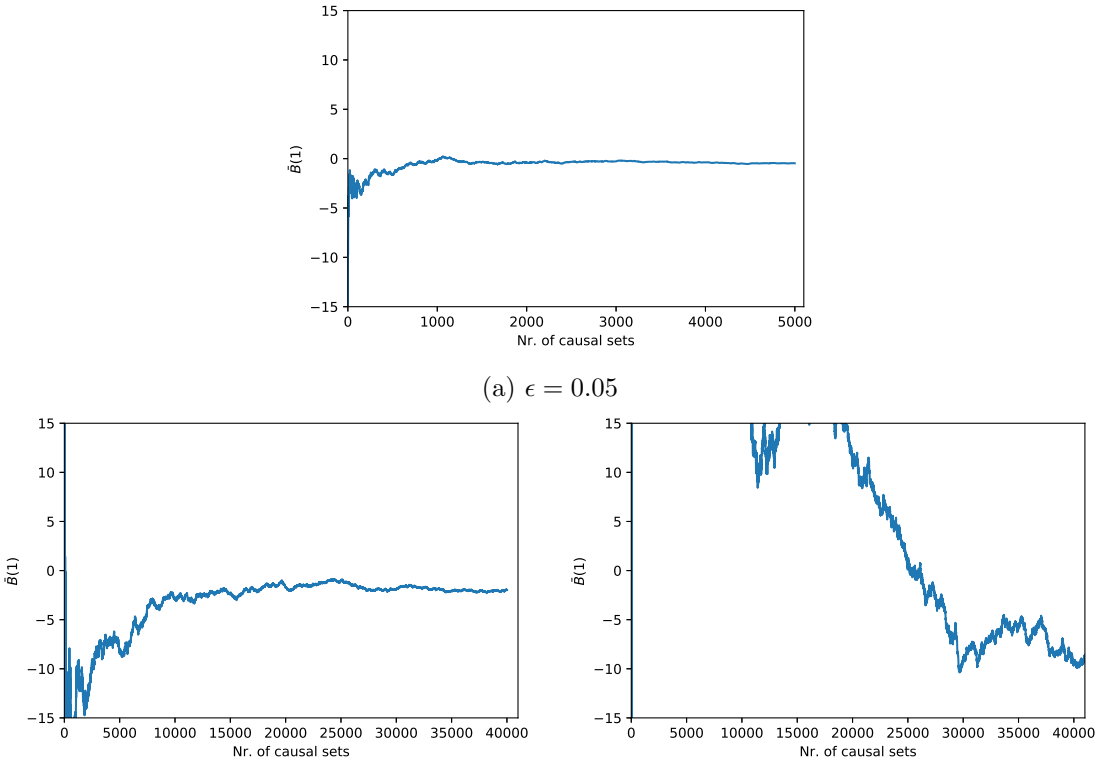

(a) $\epsilon = 0.05$

(b) $\epsilon = 0.2$

(c) $\epsilon = 0.5$

Fig. 5.3: Evolution of $\bar{B}(1)$ over an increasing number of causal sets for different ϵ. Sprinkling performed in a two-dimensional cone with depth $\tau = 1$ in Minkowski space.

5.4 Influence of different parameters on the simulation

When running the simulations there are a few parameters that have to be chosen beforehand. This includes the type and dimension of the space-time and space-time region one wants to sprinkle in, the number of elements in the causal set, which is in turn determined by the causal set density and the size of the region one sprinkles in, and the smearing factor ϵ one wants to use. To choose the right parameter for the simulations a few tests were done. The dimension was set to two and the tests where performed in Minkowski space.

The first test shows the impact the smearing has on the convergence. Figure 5.3 shows how the average $\bar{B}(1)$ of the Causal Set d'Alembertian with $\phi(x) = 1$ evolves with increasing number of causal sets for different ϵ. For a really strong smearing of $\epsilon = 0.05$, which would correspond to a ratio of the fundamental length scale of the causal set and

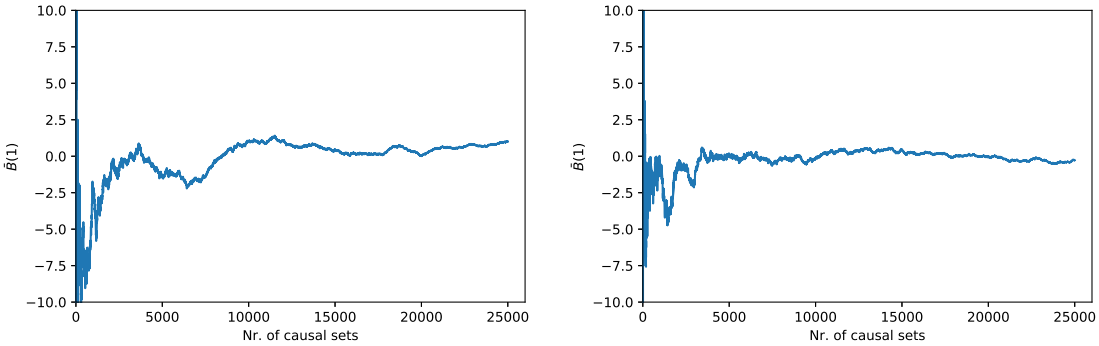

(a) diamond, $\tau = 2$, $\rho = 250$, $N = 500$

(b) cone, $\tau = 1$, $\rho = 250$, $N = 250$

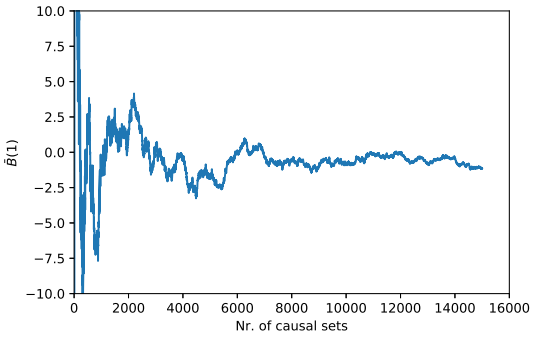

(c) diamond, $\tau = \sqrt{2}$, $\rho = 500$, $N = 500$

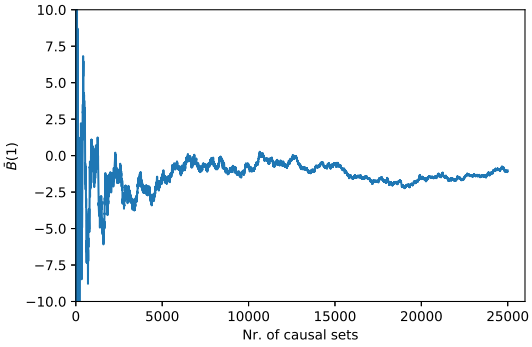

(d) cone, $\tau = 1$, $\rho = 500$, $N = 500$

Fig. 5.4: Evolution of $\bar{B}(1)$ over an increasing number of causal sets for different forms of the sprinkling region. Type and depth of the sprinkling region as well as density and resulting average number of elements in the causal set are stated below the graphs. The upper row compares a causal diamond with a cone which is the upper half of this diamond. The lower row compares a diamond with a cone of the same volume. Sprinklings performed in 2-dimensional Minkowski space and with smearing of $\epsilon = 0.2$.

the meso-scale l_k of $\frac{l}{l_k} \approx 0.22$, the average converges already after a few thousand causal sets are taken into account. For $\epsilon = 0.2$ and $\epsilon = 0.5$ the progression is shown for the first 40 thousand causal sets each. As one can see in the case $\epsilon = 0.5$ this is not enough for the average to converge. Without any smearing ($\epsilon = 1$) the fluctuations become so big that it is not possible to show them in a graph with the same scaling. These simulations where performed with a cone of depth 1 as sprinkling region and $\rho = 500$.

When checking whether a cone or a diamond are better for the simulation, no major differences where found. Figure 5.4 shows the convergence for different causal diamonds and cones. 5.4a and 5.4b compare the convergence in a diamond with a cone which is just the upper half of this diamond. 5.4c and 5.4d show the convergence behavior for a

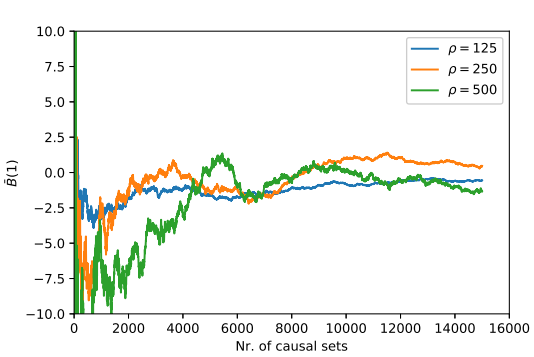

(a) Evolution of $\bar{B}$ with an increasing number of causal sets taken into account.

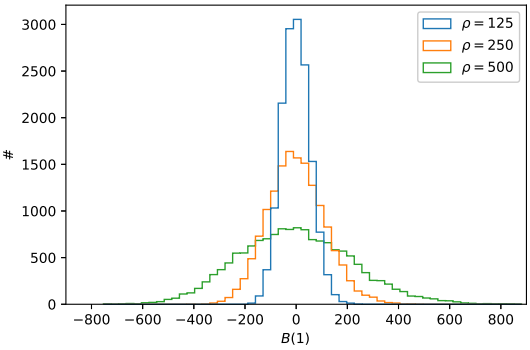

(b) Histogram with 55 bins of the value of $B(1)$ for 15000 causal sets each.

Fig. 5.5: Simulation results for sprinkling in a two-dimensional causal diamond in Minkowski space for different ρ. The size of the diamond was adapted such that the average number of elements in the causal set stays at $N = 500$. $\epsilon = 0.2$

diamond and a cone with the same volume.

The most crucial choice one has to make is the number of elements one wants to be in the sprinkling. When choosing the size of the region to sprinkle in, one is constraint in space-times which are not Minkowski, because the region should be small compared to the curvature of space-time. Therefore the main parameter that determines the number of elements is the density ρ.

A higher density reduces corrections to the continuum result and systematic errors. But a higher ρ also increases the statistical fluctuations. Remember that this is the reason smearing was introduced. To highlight the effect ρ has on the fluctuations, figure 5.5 shows the results of simulations where the number of elements was held fixed but ρ was changed. It shows how the average of $B(\phi = 1)$ develops for an increasing number of causal sets and how the individual values are distributed.

Increasing the number of elements leads to another problem, because, as discussed before, it also increases computation time drastically. This gets additionally amplified due to the increased fluctuations causing the need for more causal sets to be generated. One therefore has to find a balance between accuracy and computation time.

The final test is aimed at finding out what the minimum number of elements is that should be in the causal set, such that systematic errors are small. For this sprinklings where performed in causal cones of different sizes in Minkowski space. The density ρ was held fixed. It should be noted that for Minkowski space with a constant ϕ the first order corrections are already zero and the systematic errors come from higher order

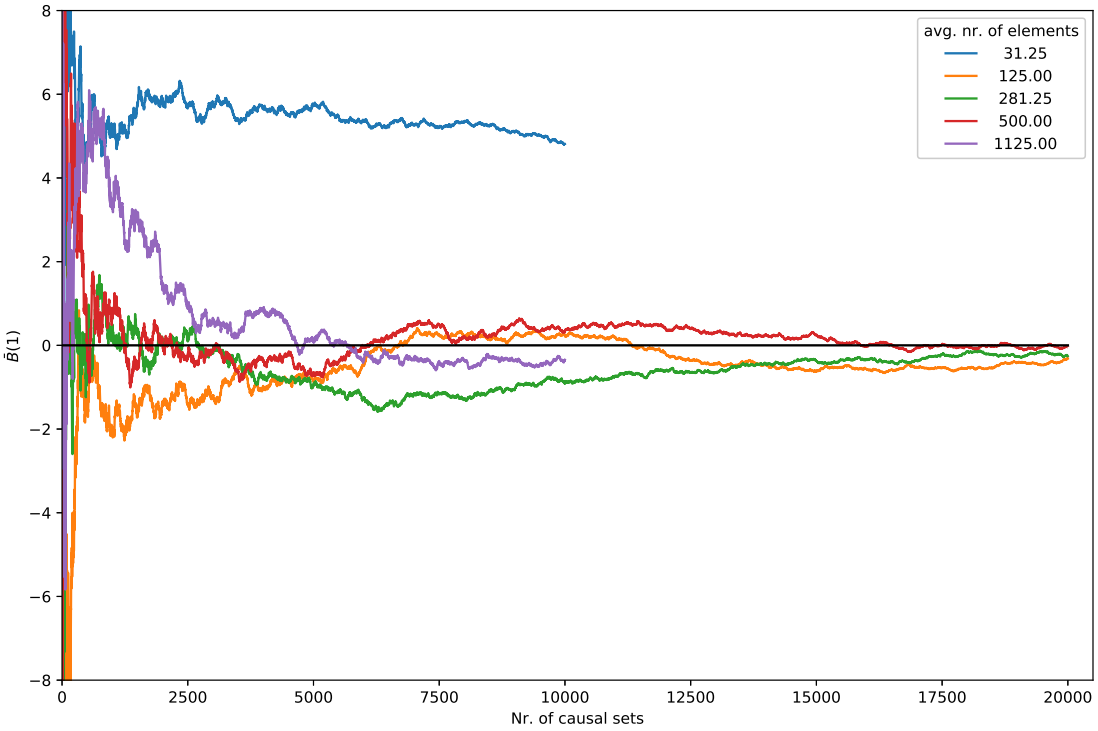

Fig. 5.6: Evolution of $\bar{B}$ with an increasing number of causal sets for causal cones in two-dimensional Minkowski space with different sizes. Density and smearing fixed at $\rho = 125$, $\epsilon = 0.2$. The black horizontal line shows the expected continuum limit.

corrections. The results are shown in figure 5.6. For an average of just 31.25 elements in the causal set (blue line) the systematic errors are much bigger than the fluctuations and the simulation was stopped after ten thousand causal sets. The simulation was also stopped at this point for cones with an average of 1125 elements in them (purple line), because the simulation already took an amount of time deemed unpractical. Indeed such a high number of elements is also not necessary as one can see that already for a smaller of elements the averages converge towards the continuum limit of zero.

5.5 Choice of parameters for the main simulation

The settings for the main simulations described in the next sections where chosen with the following rationale. For the form of the sprinkling region causal diamonds were chosen as this is what is mostly used in the literate and no major differences between the use of a cone or a diamond were found in the test. Although for the Causal Set d'Alembertian around 300 elements in the casusal set seem to be enough for the average of the operator to converge, size of the diamond and density were chosen such that the average number of elements will be 600. This is also because the B^2-operator will likely need more elements in the causal set as it gives higher weights to deeper layers.

The sprinkling region in Minkowski was set to a causal diamond with depth $\tau = \sqrt{2}$ and the density to $\rho = 600$. The de Sitter space was set to have a curvature of $R = 5$. This results in $l_c = \sqrt{\frac{d(d-1)}{R}} = \sqrt{\frac{2}{5}}$. For de Sitter space, this is the cosmological horizon.

To compare sprinklings from Minkowski and de Sitter space the causal set density and the volume of the causal diamond was held constant. This results in a constant average number of elements. The Volume of a causal diamond in Minkowski space is

$$2 \cdot \mathcal{V}(S_{d-2}) \int_0^{\frac{\tau}{2}} dt \int_0^t dr\ r^{d-2} = \frac{\mathcal{V}(S_{d-2})}{d(d-1)} \frac{\tau^d}{2^{d-1}}, \tag{5.28}$$

which in two dimensions is $\frac{\tau^2}{2}$. The volume of a causal diamond in de Sitter space is

$$2 \cdot \mathcal{V}(S_{d-2}) \int_0^{\frac{\tau}{2}} dt \int_0^{l_c \tanh \frac{t}{l_c}} dr\ r^{d-2}. \tag{5.29}$$

In two dimension this leads to $l_c^2 \ln \cosh \frac{\tau}{l_c}$. By equating the volume for Minkowski and de Sitter space one can calculate the necessary depth of the diamond in de Sitter space so that the volume stays the same. The depth of the diamond in de Sitter space was set accordingly. It's value is approximately 1.6. The maximal radius of the diamond in de

Sitter space is approximately $0.84 l_c$.

This means that the diamond is not small compared to the curvature of the space-time. Because the curvature in de Sitter is constant everywhere and the space-time is homogeneous this shouldn't be a big problem and is a necessary compromise as lowering the size of the diamond would need one to increase the density ρ to keep the average number of elements the same. This would lead to higher fluctuations in the Causal Set d'Alembertian.

If one were to extend the simulations to Anti-de Sitter space the depth of the diamond would be approximately $2l$ which is below the threshold of πl for which the maximal radius of the diamond goes to infinity. This happens because the light cone in Anti-de Sitter space can reach the boundary of space-time. Indeed the maximal radius in Anti-de Sitter space with these settings would only be around 1.

The simulation will be performed for different ϵ. In the style of [43] a step of 0.1 in the ratio between the length scale of the causal set $l = \rho^{-\frac{1}{d}}$ and the meso-scale $l_k = \rho_k^{-\frac{1}{d}}$ was mainly used. Using equal steps between 0 and 1 of $\frac{l}{l_k}$ instead of equal steps in $\frac{\rho_k}{\rho}$ relates to equal steps in $\sqrt[d]{\epsilon}$ and will result in the average epsilon being smaller then 0.25 which according to the tests is the region where the fluctuations become small enough to handle.

5.6 Results and Discussion

5.6.1 Theoretical predictions

To test if the operators $B(\phi)$ and $B^2(\phi)$ give the expected results, simulations where performed in both Minkowski and de Sitter space in two dimensions. The de Sitter space has a curvature with Ricci scalar $R = 5$ and the simulations where performed with causal set density $\rho = 600$ in a causal diamond of volume 1.

A constant ϕ with $\phi = -2$ for the B operator and $\phi = 4$ for the B^2 operator where used. For these ϕ the operators' expected values are R and R^2. To test the differential part of the operators, simulations where also performed with the scalar function $\Phi = at^2 + c$ with $a = 4$ and $c = 12$. The operators in the simulation are evaluated at the coordinate origin. For a function of the form of Φ the continuum limit of $B(\Phi(0))$ and

$B^2(\Phi(0))$ in a spacetime with constant R are

$$\lim_{\rho\to\infty} \bar{B}(\Phi(0)) = -2a - \frac{1}{2}Rc, \tag{5.30}$$

$$\lim_{\rho\to\infty} \bar{B}^2(\Phi(0)) = -R\cdot(-2a) + \frac{1}{4}R^2c. \tag{5.31}$$

The expected results for the given choice of a, c and R in the simulations are summarized in table 5.1.

	$\bar{B}(\phi=-2)$	$\bar{B}(\Phi(0))$	$\bar{B}^2(\phi=4)$	$\bar{B}^2(\Phi(0))$
Minkowski	0	−8	0	0
de Sitter	5	−38	25	115

Table 5.1: Theoratical continnum limit for $\bar{B}$ and $\bar{B}^2$ in Minkowski and de Sitter space with $R = 5$ for constant ϕ and $\Phi = 4t^2 + 12$.

5.6.2 Results for the B-operator

	$\bar{B}(\phi=-2)$	$\bar{B}(\Phi(0))$
Minkowski	−0.07	−8.25
de Sitter	4.29	−33.19

Table 5.2: Average of the B-operator with $\sqrt{\epsilon} = 0.2$ over 100 000 sprinklings in Minkowski and de Sitter space for $\phi = -2$ and $\phi = \Phi$.

The results for $\sqrt{\epsilon} = 0.2$, which shows the best convergence behavior, are summarized in table 5.2. In Minkowski space the results are in agreement with the theoretical expectations. For de Sitter significant deviations exists. It is however positive to note that the results for de Sitter clearly show the differences between different space-times and the relative error is below 15% for both cases of ϕ. It would be interested to compare the results with a more detailed theoretical prediction that takes corrections for finite causal set density into account.

Figure 5.7 shows how the average of the operator B with $\phi = -2$ evolves with an increasing number of sprinklings taken into account. One should keeps in mind that these kinds of graphs highly depend on the order in which the different sprinklings are included in the average. The fluctuations increase with increasing ϵ and for $\epsilon = 1$ one is still far from convergence.

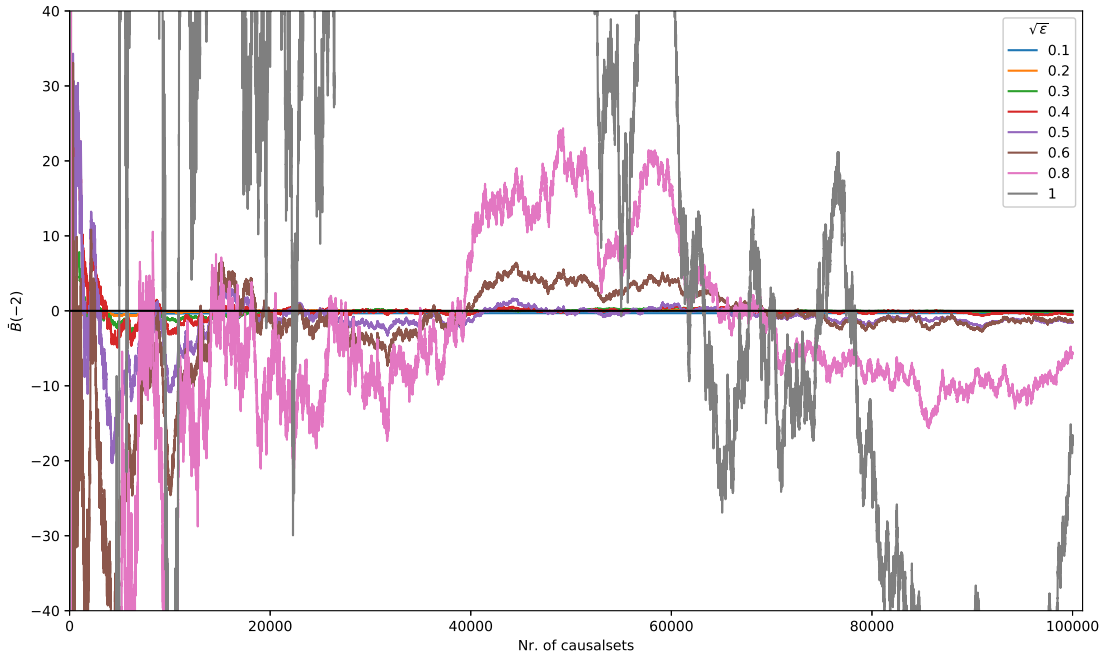

Fig. 5.7: Evolution of the average value of the operator $B(\phi = -2)$ in Minkowski space with increasing number of causal sets for different smearing factors. The theoretical value of the continuum limit is shown as a horizontal black line.

In figure 5.8a and in the following figures only results for $\sqrt{\epsilon} \leq 0.6$ are shown. Here one can now see that the average converges towards the theoretical value of zero as expected. It is however still visible that the fluctuations grow with growing ϵ and that more sprinklings need to be included in the average for all lines to converge. It is expected that with more causal sets all curves will eventually converge towards zero.

The exception here is $\sqrt{\epsilon} = 0.1$ (light blue line) which shows the best convergence but has converged on a value of approximately 0.3. The stronger the smearing is, the more layers in the causal set are needed to achieve the necessary cancellations. In the case of $\sqrt{\epsilon} = 0.1$ the deviation from zero is therefore likely due to the smearing being too strong to give a good result with the finite number of elements in the causal diamond used for the simulations. This deviation for $\sqrt{\epsilon} = 0.1$ also appears in all of the following results.

Except for this case the final average over 100 000 sprinklings gets closer to the theoretical value for smaller ϵ, which converge faster. The smallest deviation is achieved by $\sqrt{\epsilon} = 0.2$ and only deviates by about 0.07 from zero.

The results for the B-operator with $\phi = \Phi$ are shown in figure 5.8b. One should notice

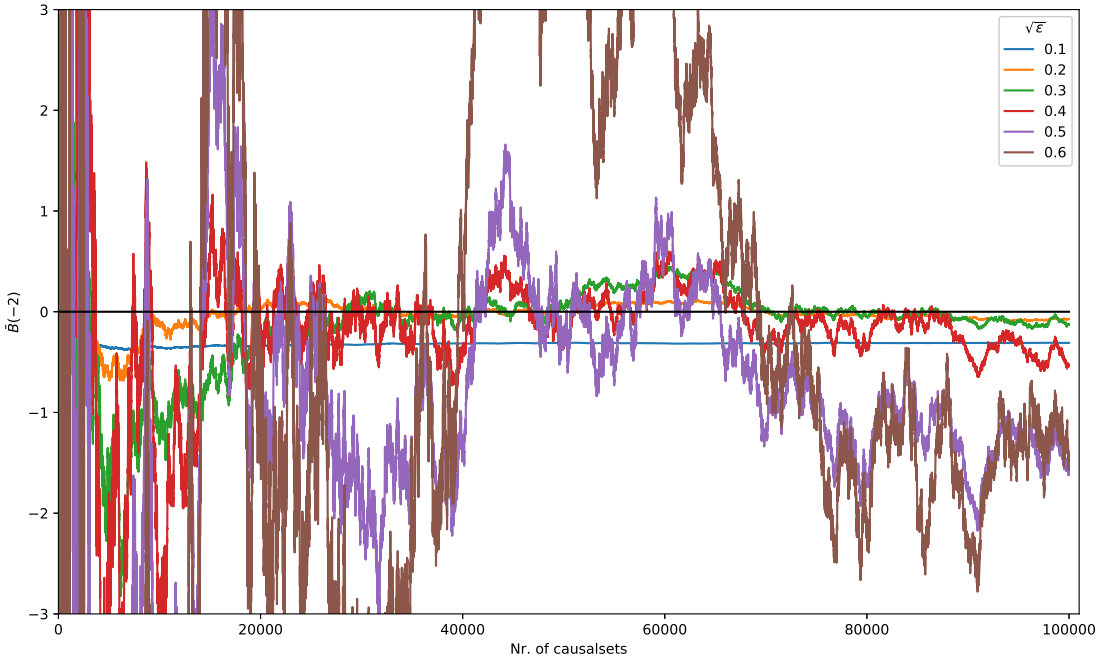

(a) $\phi = -2$

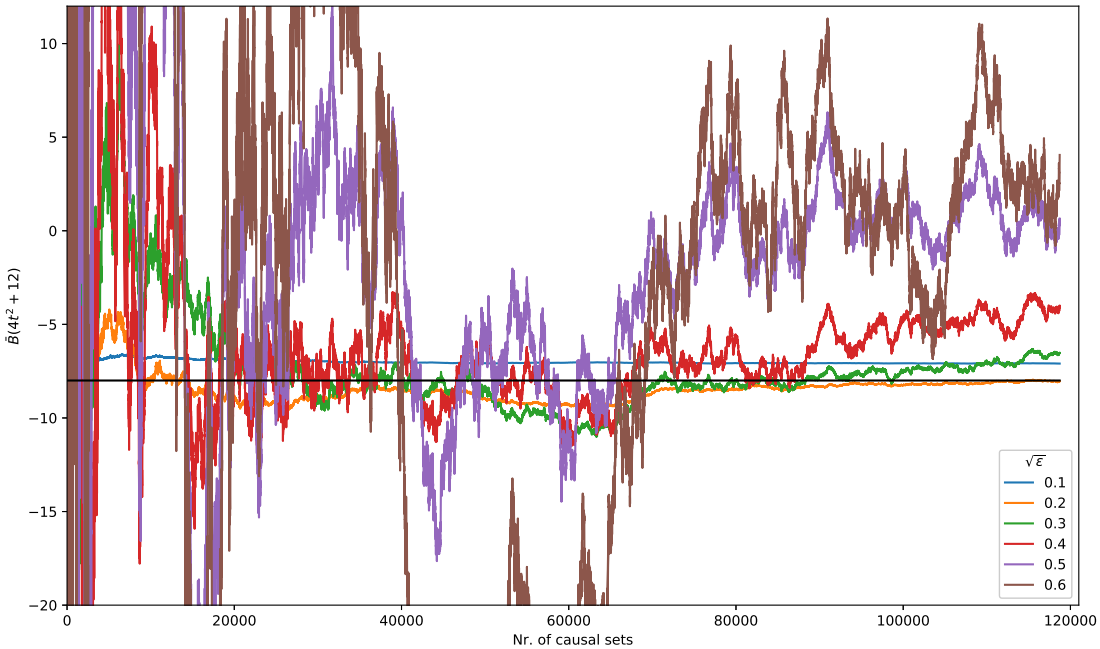

(b) $\phi = \Phi = 4t^2 + 12$

Fig. 5.8: Evolution of the average of the operator $B(\phi)$ in Minkowski space with increasing number of causal sets for different ϵ. Theoretical limit shown as horizontal black line.

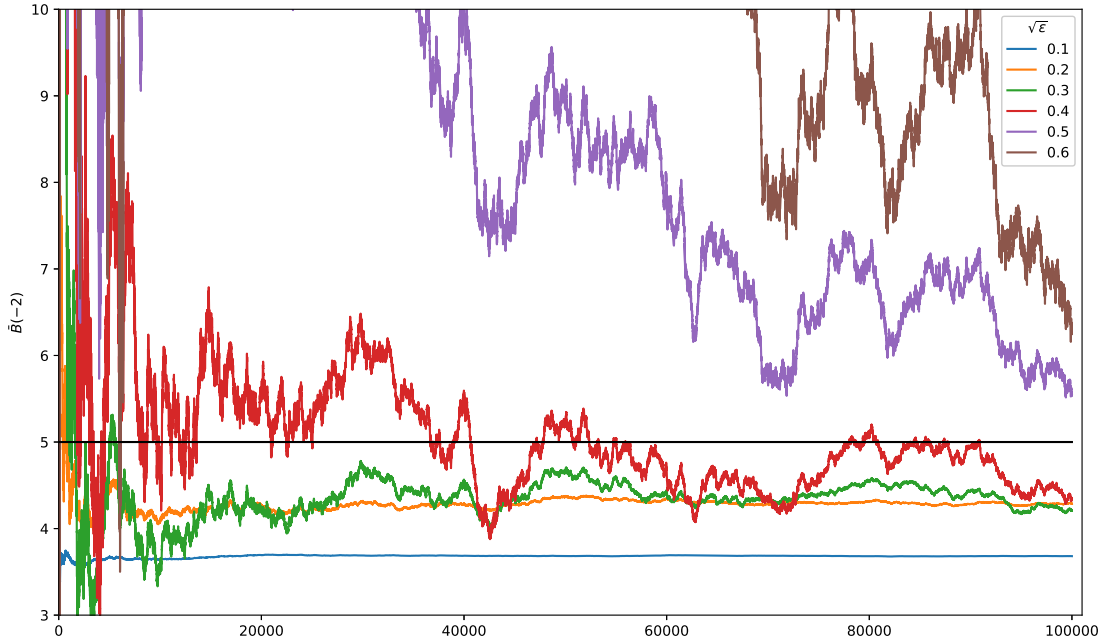

(a) $\phi = -2$

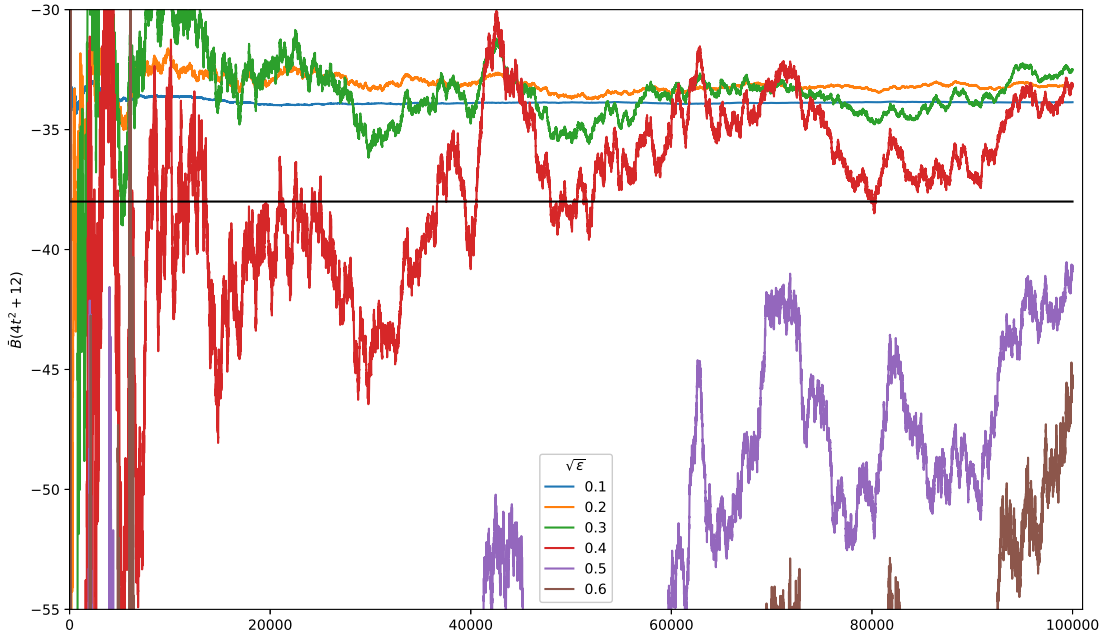

(b) $\phi = \Phi = 4t^2 + 12$

Fig. 5.9: Evolution of the average of the operator $B(\phi)$ in de Sitter space with increasing number of causal sets for different ϵ. Theoretical limit shown as horizontal black line.

the different scaling of the y-axis between different plots. The fluctuations are bigger then for the constant $\phi = -2$. Again the deviations are bigger for bigger ϵ and $\sqrt{\epsilon} = 0.2$ yields the value closest to the expectations as the average over 100 000 causal sets only deviates from the expected value of -8 by about 0.25.

The increased fluctuations for Φ compared to $\phi = -2$ are expected and can be explained as follows: Because B is linear in ϕ one can image the value of $B(\Phi = at^2 + c)$ as composed of $B(at^2) + B(c)$. The fluctuations will be a sum of the fluctuations of these two parts and the individual fluctuations from $B(at^2)$ and $B(c)$ can get enhanced or cancel each other out. If one only had $B(c = 12)$ one would expect an 6-fold increase of the fluctuations compared to $B(-2)$, because a constant ϕ only acts as an overall factor for the operator. For the $B(at^2)$ part such an estimation is not possible to make so easily, because the additional dependents of ϕ on the position of the causal set elements will likely increase the fluctuations. When comparing the fluctuations between $B(-2)$ and $B(\Phi)$ as measured by the standard deviation of the values of the operator it turn out that the increase is about 6.2-fold.

Both the results for $\phi = -2$ and $\phi = \Phi$ were always created from the same sprinklings. In figure 5.8a and 5.8b one can see this as, except for the sign, the fluctuations look very similar in both cases.

The corresponding results for de Sitter space are shown in figures 5.9a and 5.9b. The results show a clear tendency towards the expected values, they converge however on values which clearly deviate from them. For $\phi = -2$, where the theoretical limit is 5, the averages (except for $\sqrt{\epsilon} = 0.1$) converge at approximately 4.3 and for the field Φ where the theoretical limit is -38 they converge at approximately -33.2.

It would be interesting to calculate the first order finite ρ corrections to the Causal Set d'Alembertian in de Sitter space and compare their value with these deviations. For this both the integral in the near region and in the light cone region would need to be evaluate in more detail for this space-time.

The deviations are in the same direction as those for $\sqrt{\epsilon} = 0.1$, which can be seen as an indication that they at least in part come from the finiteness of the sprinkling region. Including more sprinklings to see the convergence for higher ϵ could tell how much the results improve when the operator is less smeared.

The fact that the averages for bigger ϵ converge from a specific direction has no meaning, because this depends on in which order the average is taken. This can be seen in figure 5.10, which shows the same results as figure 5.9a but the values of B on the individual causal sets were included in the average in a different order.

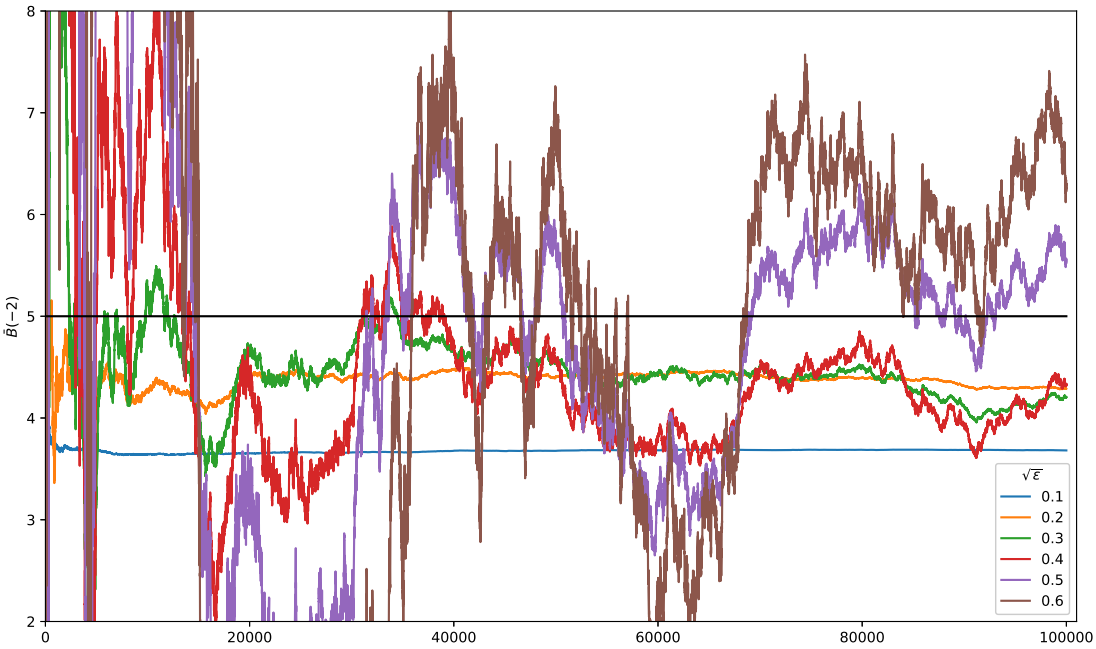

Fig. 5.10: Evolution of the average of the operator $B(\phi = -2)$ in de Sitter space with increasing number of causal sets for different ϵ. Theoretical limit shown as horizontal black line. This figure shows the same results as 5.9a but the average was taken over the values in a different order.

The fluctuations are bigger for de Sitter space then Minkowski space. Overall they show the same tendencies as in Minkowski-space, in the sense that the fluctuations and the number of causal sets needed for convergence get smaller for smaller ϵ with the exception of $\sqrt{\epsilon} = 0.1$, and that the fluctuations for $B(\Phi)$ show a similar pattern but increases magnitude compared to $B(-2)$.

5.6.3 Results for the B^2-operator

	$\bar{B}^2(\phi = 4)$	$\bar{B}^2(\Phi(0))$
Minkowski	11.3	72.6
de Sitter	43.0	187.0

Table 5.3: Average of the B^2-operator with $\sqrt{\epsilon} = 0.2$ over 100 000 sprinklings in Minkowski and de Sitter space for $\phi = 4$ and $\phi = \Phi$.

The results for the B^2-operator are summarized in table 5.3. Smearing was applied to both the inner and the outer B operator in B^2 equally. The fluctuations are much

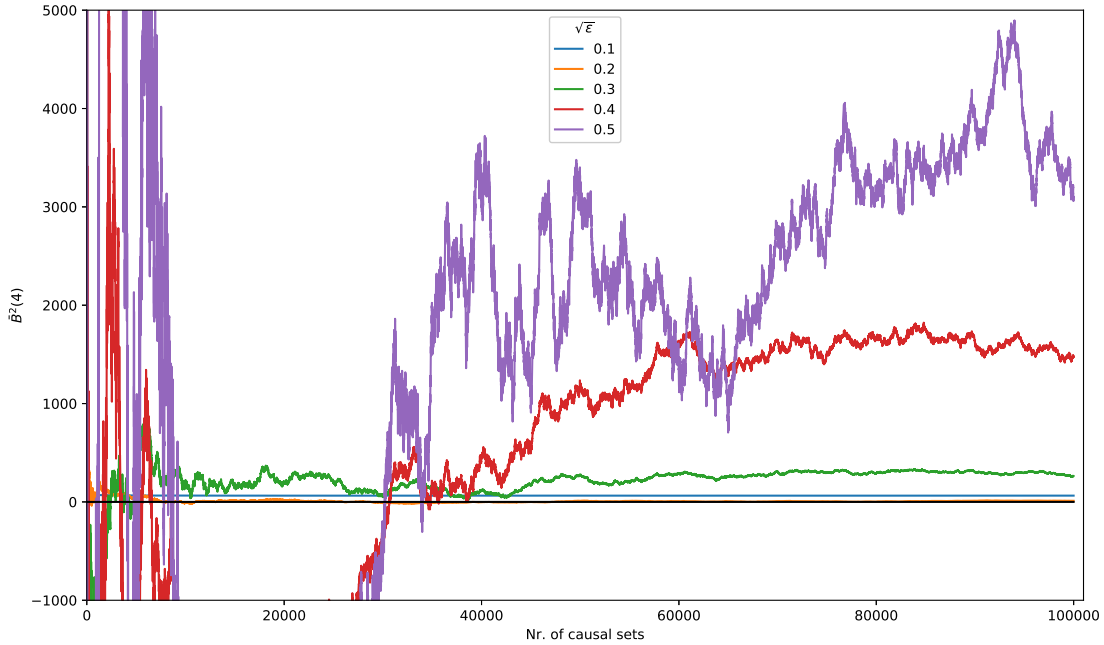

(a) $\phi = 4$

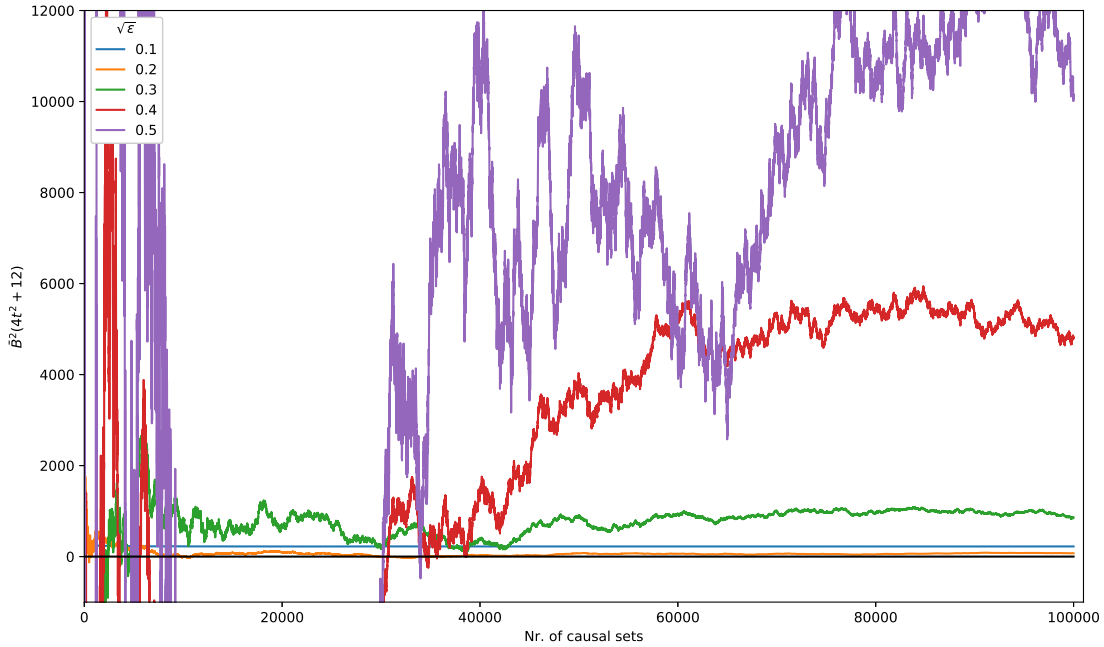

(b) $\phi = \Phi = 4t^2 + 12$

Fig. 5.11: Evolution of the average of the operator $B^2(\phi)$ in Minkowski space with increasing number of causal sets for different ϵ. Theoretical limit shown as horizontal black line.

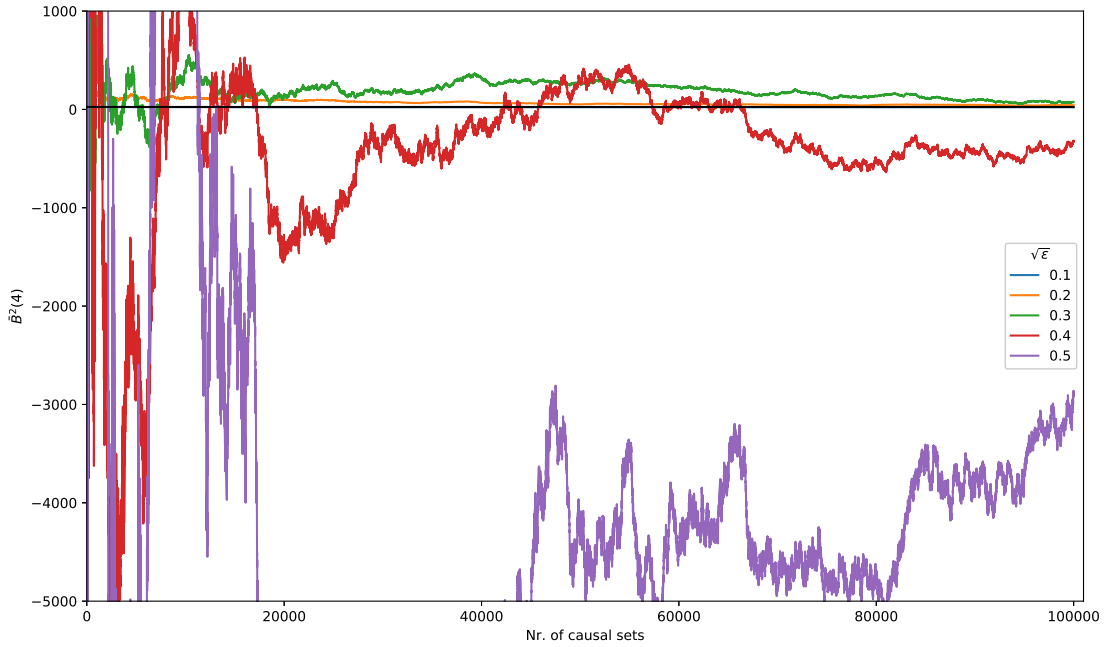

(a) $\phi = 4$

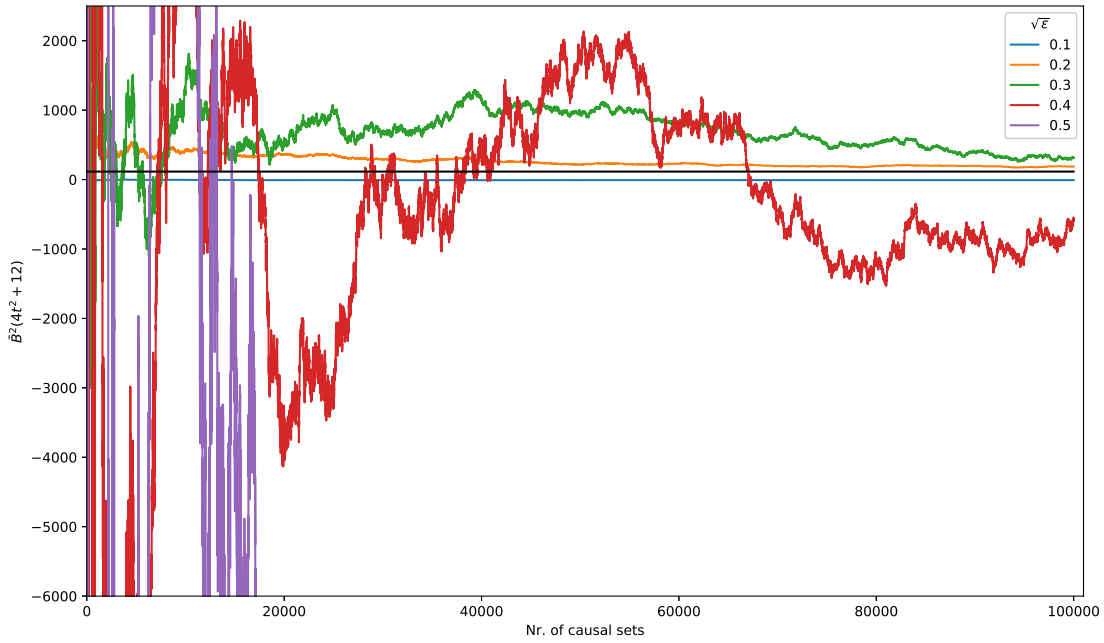

(b) $\phi = \Phi = 4t^2 + 12$

Fig. 5.12: Evolution of the average of the operator $B^2(\phi)$ in de Sitter space with increasing number of causal sets for different ϵ. Theoretical limit shown as horizontal black line.

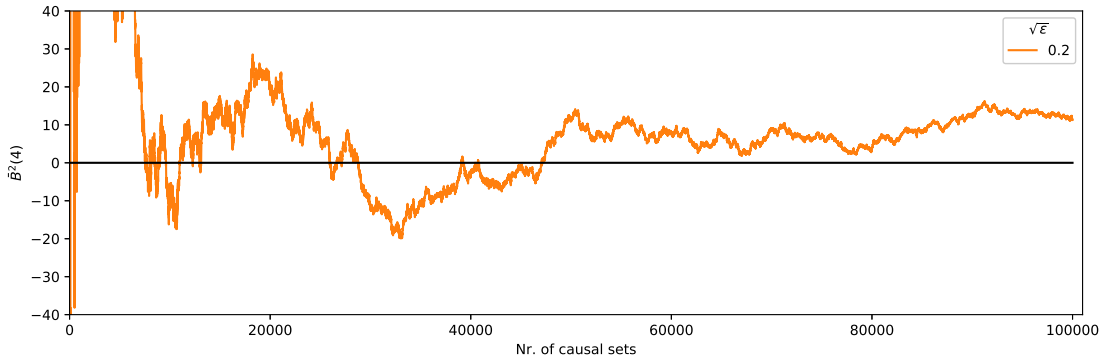

(a) Minkowski, $\phi = 4$

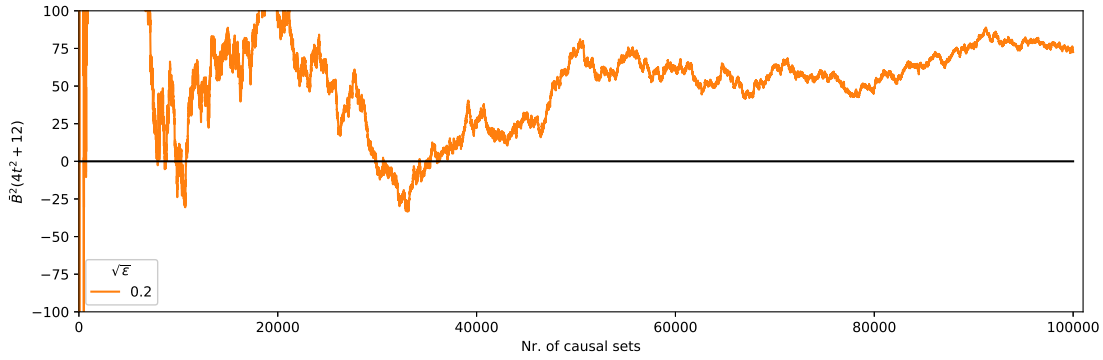

(b) Minkowski, $\phi = \Phi = 4t^2 + 12$

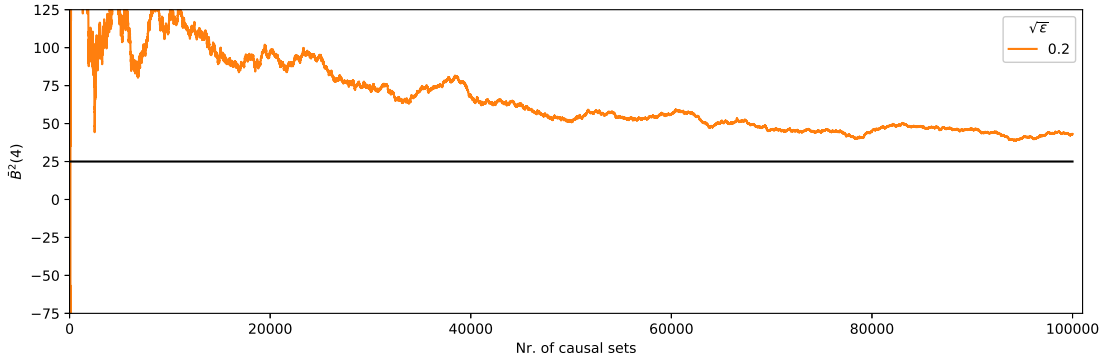

(c) de Sitter, $\phi = 4$

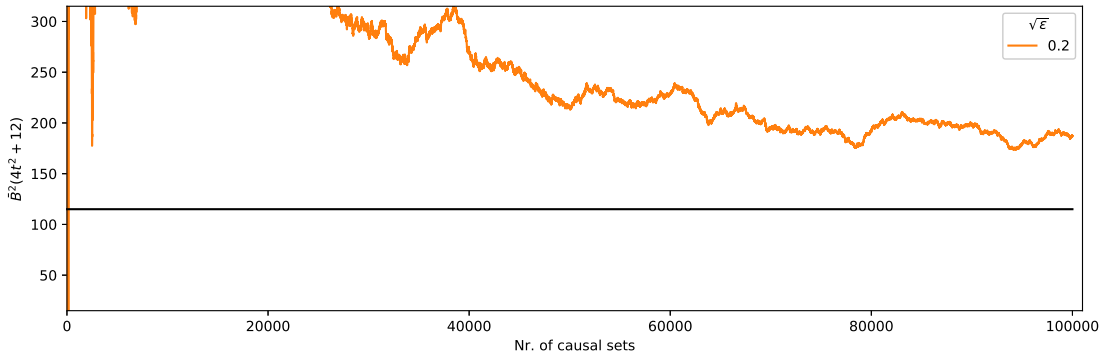

(d) de Sitter, $\phi = \Phi = 4t^2 + 12$

Fig. 5.13: Evolution of the average of the operator $B^2(\phi)$ in Minkowski and de Sitter space with increasing number of causal sets for $\sqrt{\epsilon} = 0.2$. Theoretical limits are shown as horizontal black line.

bigger than for the B-operator and the average after 100 000 sprinklings deviates much more from the expected values. It is likely that due to the higher fluctuations much more causal sets need to be included into the average before a real convergence can be seen.

The fluctuations show the same pattern as before in the sense that the errors get smaller for smaller ϵ with the exceptions of $\sqrt{\epsilon} = 0.1$, which again converges at a value away from the predicted result. The best result is again achieved with $\sqrt{\epsilon} = 0.2$. Also one can again see that the fluctuations behave similar for different ϕ when the results were generated from the same sprinklings.

The exact increase in the size of the fluctuations compared to the B-operator as measured by the standard deviation depends on ϵ and is bigger for bigger ϵ. In Minkowski space it reaches from around 130-fold to around 1120-fold for $\sqrt{\epsilon}$ between 0.2 and 0.5 and for de Sitter from around 67-fold to around 630-fold for the same range of ϵ.

B^2 is effectively like applying the B-operator twice. Therefore also the systematic errors get amplified as can be seen from increasing deviations for $\sqrt{\epsilon} = 0.1$ from the theoretical result. The average increase is 23.4-fold.

The convergence of the average in Minkowski space is shown in figures 5.11a and 5.11b. Only the results for $\sqrt{\epsilon} \leq 0.5$ are drawn, because of the high fluctuations for bigger ϵ. The final result for $\sqrt{\epsilon} = 0.2$, which is closest to the theoretical value of zero, is approximately 11.3 for $\phi = 4$ and approximately 72.6 for $\phi = \Phi$. The evolution of the average for $\sqrt{\epsilon} = 0.2$ is shown again in figure 5.13a and 5.13b.

For de Sitter space the results are shown in figure 5.12a and 5.12b as well as in 5.13c and 5.13d for $\sqrt{\epsilon} = 0.2$. The average for $\sqrt{\epsilon} = 0.2$ over 100 000 sprinklings is 43 (vs 25 expected) for $\phi = 4$ and 187 (vs 115 expected) for $\phi = \Phi$. The fluctuations are again bigger in de Sitter space than those for Minkowski space. Also one can see from figure 5.13c and 5.13d that the average has still not converged yet.

5.6.4 Increase of fluctuations with ϵ

It was evident in the results that the fluctuations drastically increase with increasing $\sqrt{\epsilon}$. It was therefore interesting to ask weather there is a relationship between these two. Indeed the standard deviation of the values of an operator on different causal sets seems to increase polynomially with $\sqrt{\epsilon}$. This can be seen in the log-log-plot of these two quantities for the B operator in Minkowskispace in figure 5.14.

Doing the same analysis for the other simulations showed that this relation between

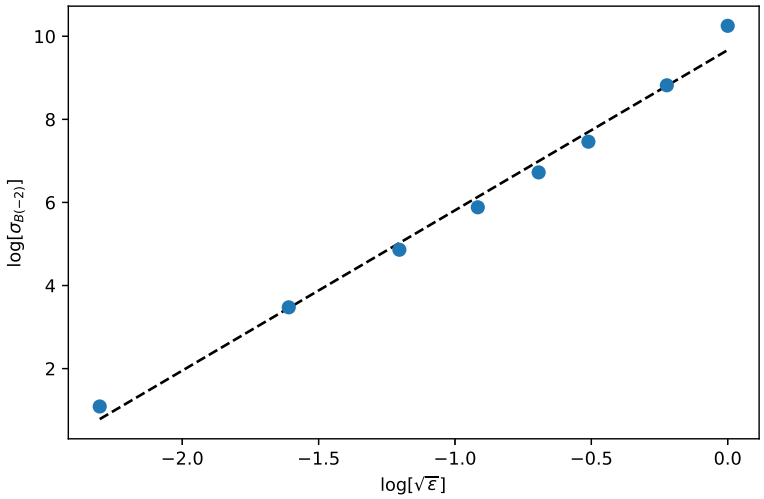

Fig. 5.14: Log-log-plot of $\sqrt{\epsilon}$ and the standard deviation of the value of $B(-2)$ in Minkowski space. The linear regression line has a slope of ca. 3.86

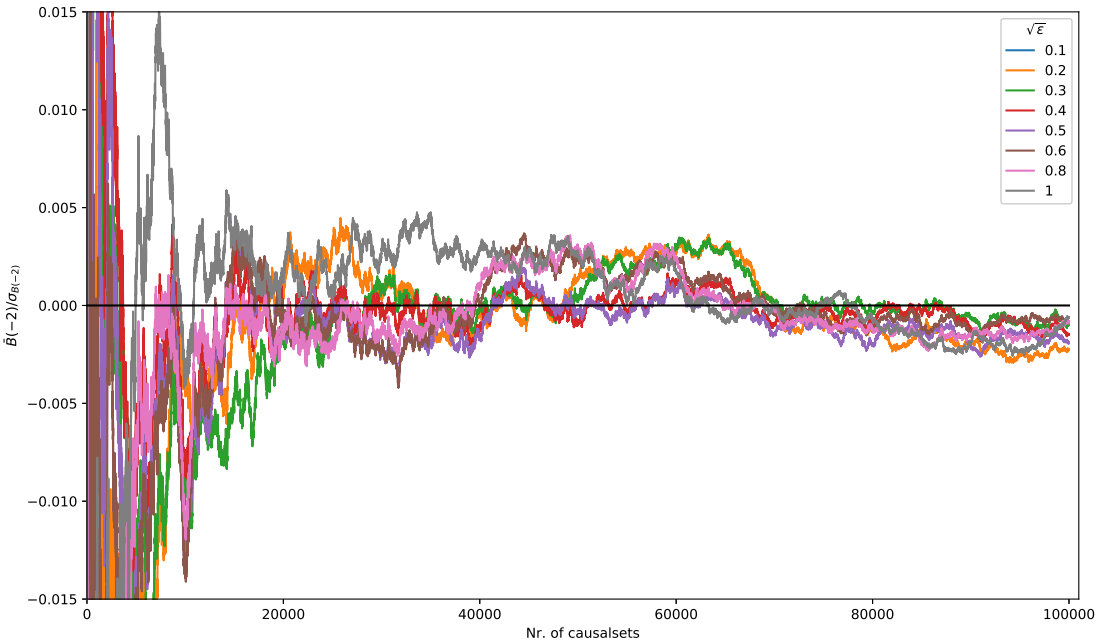

Fig. 5.15: Evolution of the average value of the operator $B(\phi = -2)$ divided by the standard deviation of B in Minkowski space with increasing number of causal sets for different ϵ. The theoretical value of the continuum limit is shown as a horizontal black line.

the size of the fluctuations and the ϵ parameter does only depend on the operator and not on the space-time or on the function of ϕ. The average power of $\sqrt{\epsilon}$ with which the fluctuations increase for the B-operator is approximately 3.7 and for the B^2 operator it is approximately 5.9.

When dividing the values by the standard deviation the convergence of the average is similar for all ϵ as can be seen from figure 5.15. Therefore knowing the relations between smearing and the fluctuations could help to predict how many causal sets are needed until the average of the operator converges to a certain precision for a given ϵ.

Chapter 6

Conclusion and Outlook

In order to be able to better describe the emergent space-time from causal sets and to connect the theory with other Quantum Gravity approaches it is important to find operators which provide information about the curvature of the emergent manifold beyond the Ricci-scalar R. This thesis uses the Causal Set d'Alembertian to work towards this goal.

First an extended a proof of the continuum limit for the Causal Set d'Alembertian $B(\phi(x))$ in general curved space-times of arbitrary dimension was presented in chapter 3, which extends the current proofs of the Causal Set d'Alembertian in the literature. The Causal Set d'Alembertian was then used to define a new operator $B^2(\phi(x))$ for causal sets in chapter 4. The new operator resembles the composition of two Causal Set d'Alembertians and contains both R^2 and $\Box R$ in its continuum limit.

For both the Causal set d'Alembertian and the new operator numerical simulations have been performed in two-dimensional Minkowski and de Sitter space-time. The simulations show some deviations from the expected result in the average of the value of these operators over multiple sprinklings. It is expected that this divergence between theory and simulations can be resolved by averaging over more causal sets and taking corrections to the continuum result into account. It would be interesting to see if this in indeed the case.

Nonetheless, the averages seem to generally converge towards the theoretical values, which can be taken as a sign for the correctness of the predictions in the limit of high density ρ. Yet, the convergence is plagued by high fluctuations of the operator values, which have to be tamed using smearing. Arbitrary strong smearing is however not possible as this increases systematic errors from the finiteness of the sprinkling used. A possible future line of research for this kind of simulations is to find the optimal balance for the density ρ and the smearing parameter ϵ.

Further possible extensions of the simulations include simulations in higher dimensions and in other space-times, for example Anti-de Sitter space. It would also be useful to

be able to sprinkle causal sets in arbitrary space-times, but this is difficult, because one has to calculate for each pair of elements if they are space-like or causally separated.

The new operator B^2 can be used to get a value for the combination of $R^2 - 2\Box R$ and generalizations of it in the form of $B^n = B \circ B \circ \ldots \circ B$ yield higher order combinations of R and $\Box$. To disentangle R^2 and $\Box R$ another operator has to be used. It is expected that from an operator of the form $[B(\phi)]^2$ one can extract R^2 directly [61]. First simulations indicate that this is indeed the case. With this it would be conceivable to build an action for causal sets that contains terms for R, R^2 and $\Box R$ separately. A more general action would allow for new possibilities in the search of a second order phase transition in the space of couplings in Causal Sets. Such a phase transition would have implications for Quantum Gravity outside of Causal Sets and would make a case for Asymptotic Safety in a Lorentzian setting.

It would also be interesting to find a way of attaining other components of the Ricci- or Riemann-tensor from causal sets and compare results for different curvature quantities from different methods to get a criterion for the manifold-likeness of a causal set. In [18] an alternative method to extract R and R_{00} from a causal set was presented. It seems also possible to use the construction of space-like distances for causal sets in [21] to construct a causal diamond out of a geodesic ball and use the results from [62] for this "geodesic ball causal diamond" and the usual Alexandrov interval causal diamond, defined through the time-like distance from its start- to endpoint, to get a measure for R and R_{00}. With the simultaneous construction of a geodesic ball and Alexandrov interval causal diamond it would also already be possible to get some information about the Weyl tensor in flat space-times [62].

Extensions towards other components of the Ricci-tensor are not possible within the framework of the Causal Set d'Alembertian alone. Such components could come from higher orders in the metric expansion in Riemann Normal Coordinates, but such terms of the corrections to the Causal Set d'Alembertian would be of at least the same order in ρ as the corrections from the light-cone region. There an expansion of volume $\mathcal{V}(x, y)$, needed to calculate the contributions from this region, is not yet as easily possible. A possibly exciting way to continue research in this direction would be to check if other curvature components can be extracted from higher order expansions in the other two methods of attaining R from the causal set.

In summary it can be said that the results from this thesis open the path to further research in the direction of curvature operators for Causal Set Theory. Especially the prospect of construction more complex actions for Causal Set dynamics could lead to

important findings in the context of Quantum Gravity.

Appendix A

Application of $\mathcal{O}_d$ on $\rho^{l-\lambda}\gamma\left(\lambda, b\rho\right)$

In this section the result

$$\begin{aligned}&\mathcal{O}_{2n}\frac{\gamma(\lambda,b\rho)}{\rho^{\lambda-l}}\\&=\frac{1}{2^{n+1}(n+1)!}\left[A_{\lambda,l}(n)\frac{\gamma(\lambda,b\rho)}{\rho^{\lambda-l}}+\sum_{k=0}^{n}(-1)^k B_{\lambda,l}(k+1,n)d^{1+k}b^{\lambda+k}\rho^{l+k}e^{-b\rho}\right]\end{aligned}\tag{A.1}$$

with

$$A_{\lambda,l}(n):=\prod_{j=0}^{n}\left(d(l-\lambda)+2j+2\right),\tag{A.2}$$

$$B_{\lambda,l}(m,n):=\begin{cases}A_{\lambda,l}(n),\text{if } m=0\\1,\text{if } m=n+1\\B_{\lambda,l}(m,n-1)\left(d(l+m-1)+2n+2\right)+B_{\lambda,l}(m-1,n-1),\text{otherwise}\end{cases}\tag{A.3}$$

will be proven by induction. For this first check the correctness of equation (A.1) for $n=0$:

$$\mathcal{O}_0\frac{\gamma(\lambda,b\rho)}{\rho^{\lambda-l}}=\frac{(d\rho\partial_\rho+2)}{2}\frac{\gamma(\lambda,b\rho)}{\rho^{\lambda-l}}.\tag{A.4}$$

Using

$$\frac{\partial}{\partial\rho}\gamma(\lambda,b\rho)=b^\lambda\rho^{\lambda-1}e^{-b\rho}\tag{A.5}$$

this gives

$$\frac{1}{2}\left[(d(l-\lambda)+2)\,\frac{\gamma(\lambda,b\rho)}{\rho^{\lambda-l}}+db^{\lambda}\rho^{l}e^{-b\rho}\right] \tag{A.6}$$

$$=\frac{1}{2}\left[A_{\lambda,l}(0)\frac{\gamma(\lambda,b\rho)}{\rho^{\lambda-l}}+B_{\lambda,l}(1,0)db^{\lambda}\rho^{l}e^{-b\rho}\right]. \tag{A.7}$$

Next follows the induction step to show that when equ. (A.1) is true for n it is also true for $n+1$. The differential operator for $n+1$ is given by

$$\mathcal{O}_{2(n+1)}\frac{\gamma(\lambda,b\rho)}{\rho^{\lambda-l}}=\frac{(d\rho\partial_\rho+2)\cdots(d\rho\partial_\rho+2(n+1)+2)}{2^{n+2}(n+2)!}\frac{\gamma(\lambda,b\rho)}{\rho^{\lambda-l}}. \tag{A.8}$$

The order of the terms of the operator $\mathcal{O}_{2n}$ can be interchanged. After moving the term with $n+1$ to the front one has

$$\frac{(d\rho\partial_\rho+2(n+1)+2)}{2(n+2)}\mathcal{O}_{2n}\frac{\gamma(\lambda,b\rho)}{\rho^{\lambda-l}} \tag{A.9}$$

$$=\frac{(d\rho\partial_\rho+2(n+1)+2)}{2(n+2)}\frac{1}{2^{n+1}(n+1)!}$$
$$\left[A_{\lambda,l}(n)\frac{\gamma(\lambda,b\rho)}{\rho^{\lambda-l}}+\sum_{k=0}^{n}(-1)^{k}B_{\lambda,l}(k+1,n)d^{1+k}b^{\lambda+k}\rho^{l+k}e^{-b\rho}\right]. \tag{A.10}$$

Now applying the last differential and thereafter using the definitions for $A_{\lambda,l}(n)$ and $B_{\lambda,l}(m,n)$ this becomes

$$\frac{1}{2^{n+2}(n+2)!}\left[A_{\lambda,l}(n)\left(\left(d(l-\lambda)+2(n+1)+2\right)\frac{\gamma(\lambda,b\rho)}{\rho^{\lambda-l}}+db^{\lambda}\rho^{l}e^{-b\rho}\right)\right. \tag{A.11}$$
$$\left.+\sum_{k=0}^{n}(-1)^{k}B_{\lambda,l}(k+1,n)d^{1+k}b^{\lambda+k}\left(d(l+k-b\rho)+2(n+1)+2\right)\rho^{l+k}e^{-b\rho}\right]$$
$$=\frac{1}{2^{n+2}(n+2)!}\left[A_{\lambda,l}(n+1)\frac{\gamma(\lambda,b\rho)}{\rho^{\lambda-l}}+B_{\lambda,l}(0,n)db^{\lambda}\rho^{l}e^{-b\rho}\right.$$
$$+B_{\lambda,l}(1,n)db^{\lambda}\left(dl+2(n+1)+2\right)\rho^{l}e^{-b\rho}$$
$$+\sum_{k=1}^{n}(-1)^{k}\left[B_{\lambda,l}(k+1,n)\left(d(l+k)+2(n+1)+2\right)+B_{\lambda,l}(k,n)\right]d^{1+k}b^{\lambda+k}\rho^{l+k}e^{-b\rho}$$
$$\left.+(-1)^{n+1}B_{\lambda,l}(n+1,n)d^{2+n}b^{\lambda+n+1}\rho^{l+n+1}e^{-b\rho}\right] \tag{A.12}$$
$$=\frac{1}{2^{n+2}(n+2)!}\left[A_{\lambda,l}(n+1)\frac{\gamma(\lambda,b\rho)}{\rho^{\lambda-l}}+B_{\lambda,l}(1,n+1)db^{\lambda}\rho^{l}e^{-b\rho}\right. \tag{A.13}$$
$$+\sum_{k=1}^{n}(-1)^{k}B_{\lambda,l}(k+1,n+1)d^{1+k}b^{\lambda+k}\rho^{l+k}e^{-b\rho}$$
$$\left.+(-1)^{n+1}B_{\lambda,l}(n+2,n+1)d^{2+n}b^{\lambda+n+1}\rho^{l+n+1}e^{-b\rho}\right]$$
$$=\frac{1}{2^{n+2}(n+2)!}\left[A_{\lambda,l}(n+1)\frac{\gamma(\lambda,b\rho)}{\rho^{\lambda-l}}+\sum_{k=0}^{n+1}(-1)^{k}B_{\lambda,l}(k+1,n+1)d^{1+k}b^{\lambda+k}\rho^{l+k}e^{-b\rho}\right]. \tag{A.14}$$

This is obviously the same as

$$\frac{1}{2^{n+1}(n+1)!}\left[A_{\lambda,l}(n)\frac{\gamma(\lambda,b\rho)}{\rho^{\lambda-l}}+\sum_{k=0}^{n}(-1)^{k}B_{\lambda,l}(k+1,n)d^{1+k}b^{\lambda+k}\rho^{l+k}e^{-b\rho}\right] \tag{A.15}$$

when $n\to n+1$. ■

Appendix B

Solving the integral (3.42) for general $\mu \geq \kappa > -1$

This section is concerned with the solution to integral (3.42) from section 3.4. One has

$$\int_0^{\mathfrak{a}} dy \int_0^{\mathfrak{a}} dx \; y^{\mu} x^{\kappa} \mathcal{O}_d \rho^l e^{-\rho c_d x y} \tag{B.1}$$

and $\mu \geq \kappa > -1$.

The first step is to move the operator $\mathcal{O}_d$ outside the inner integral and then perform the integration over x to get

$$c_d^{-\kappa-1} \int_0^{\mathfrak{a}} dy \; y^{\mu-\kappa-1} \mathcal{O}_d \frac{\gamma\left(\kappa+1, \rho c_d \mathfrak{a} y\right)}{\rho^{\kappa+1-l}}. \tag{B.2}$$

Using the result from appendix A this gives, with $\mathcal{O}_d = \mathcal{O}_{2n}, n = \left\lfloor \frac{d}{2} \right\rfloor$,

$$\begin{aligned} \frac{c_d^{-\kappa-1}}{2^{n+1}(n+1)!} \int_0^{\mathfrak{a}} dy \; y^{\mu-\kappa-1} \Bigg[& A_{\kappa+1,l}(n) \frac{\gamma\left(\kappa+1, \rho c_d \mathfrak{a} y\right)}{\rho^{\kappa+1-l}} + \\ & \sum_{\iota=0}^{n} (-1)^{\iota} B_{\kappa+1,l}(\iota+1, n) d^{1+\iota} \left(c_d \mathfrak{a} y\right)^{\kappa+1+\iota} \rho^{l+\iota} e^{-c_d \mathfrak{a} \rho} \Bigg]. \end{aligned} \tag{B.3}$$

For the second term this integral can be performed straightforwardly giving another γ-function. For the first term one has to write the integral with $y = \mathfrak{a} t$ as

$$\int_0^{\mathfrak{a}} dy \; y^{\mu-\kappa-1} \rho^{l-\kappa-1} \gamma\left(\kappa+1, \rho c_d \mathfrak{a} y\right) \tag{B.4}$$

$$= \mathfrak{a}^{\mu-\kappa} \int_0^1 dt \; t^{\mu-\kappa-1} \rho^{l-\kappa-1} \gamma\left(\kappa+1, \rho c_d \mathfrak{a}^2 t\right) \tag{B.5}$$

$$= \mathfrak{a}^{\mu-\kappa} \left(c_d \mathfrak{a}^2\right)^{\kappa+1} \int_0^1 dt \; t^{\mu} \rho^l \frac{\kappa+1}{\kappa+1} \left(c_d \mathfrak{a}^2 t \rho\right)^{-\kappa-1} \gamma\left(\kappa+1, \rho c_d \mathfrak{a}^2 t\right). \tag{B.6}$$

Now one can use [52]

$$\frac{s}{z^s} \gamma(s, z) = {}_1F_1\left(\begin{matrix} s \\ s+1 \end{matrix} \middle| -z \right) \tag{B.7}$$

to write this as

$$\mathfrak{a}^{\mu-\kappa}\left(c_d\mathfrak{a}^2\right)^{\kappa+1}\frac{1}{\kappa+1}\int_0^1 dt\ t^{\mu}\rho^l\,{}_1F_1\left(\begin{matrix}\kappa+1\\ \kappa+2\end{matrix}\middle|\,-\rho c_d\mathfrak{a}^2 t\right). \tag{B.8}$$

After expanding as

$$\begin{aligned}\frac{\mathfrak{a}^{\mu-\kappa}\left(c_d\mathfrak{a}^2\right)^{\kappa+1}}{\kappa+1}\rho^l\frac{\Gamma(\mu+1)\Gamma(1)}{\Gamma(\mu+2)}\frac{\Gamma(\mu+2)}{\Gamma(\mu+1)\Gamma(1)} \\ \cdot\int_0^1 dt\ t^{(\mu+1)-1}(1-t)^{\mu+2-(\mu+1)-1}\,{}_1F_1\left(\begin{matrix}\kappa+1\\ \kappa+2\end{matrix}\middle|\,-\rho c_d\mathfrak{a}^2 t\right),\end{aligned} \tag{B.9}$$

one can directly apply Euler's integral transformation [63] to solve the integral and gets

$$\frac{\mathfrak{a}^{\mu-\kappa}\left(c_d\mathfrak{a}^2\right)^{\kappa+1}}{\kappa+1}\rho^l\frac{\Gamma(\mu+1)\Gamma(1)}{\Gamma(\mu+2)}\,{}_2F_2\left(\begin{matrix}\kappa+1, & \mu+1\\ \kappa+2, & \mu+2\end{matrix}\middle|\,-\rho c_d\mathfrak{a}^2\right) \tag{B.10}$$

$$=\frac{\mathfrak{a}^{\mu+\kappa+2}c_d^{\kappa+1}}{(\kappa+1)(\mu+1)}\rho^l\,{}_2F_2\left(\begin{matrix}\kappa+1, & \mu+1\\ \kappa+2, & \mu+2\end{matrix}\middle|\,-\rho c_d\mathfrak{a}^2\right). \tag{B.11}$$

So the final result of equation (B.3) is

$$\begin{aligned}\frac{1}{2^{n+1}(n+1)!}\Bigg[A_{\kappa+1,l}(n)\frac{\mathfrak{a}^{\mu+\kappa+2}\rho^l}{(\kappa+1)(\mu+1)}\,{}_2F_2\left(\begin{matrix}\kappa+1, & \mu+1\\ \kappa+2, & \mu+2\end{matrix}\middle|\,-\mathfrak{a}^2c_d\rho\right) \\ +c_d^{-\mu-1}\mathfrak{a}^{\kappa-\mu}\rho^{l-\mu-1}\sum_{\iota=0}^{n}(-1)^{\iota}B_{\kappa+1,l}(\iota+1,n)d^{1+\iota}\gamma\left(\mu+\iota+1,\mathfrak{a}^2c\rho\right)\Bigg].\end{aligned} \tag{B.12}$$

Bibliography

[1] Astrid Eichhorn. "Asymptotically safe gravity". In: *57th International School of Subnuclear Physics: In Search for the Unexpected*. Feb. 2020. arXiv: 2003.00044 [gr-qc].

[2] Abhay Ashtekar and Eugenio Bianchi. "A short review of loop quantum gravity". In: *Reports on Progress in Physics* 84.4 (Mar. 2021), p. 042001. DOI: 10.1088/1361-6633/abed91.

[3] Carlo Rovelli and Francesca Vidotto. *Covariant Loop Quantum Gravity: An Elementary Introduction to Quantum Gravity and Spinfoam Theory*. Cambridge University Press, 2014. DOI: 10.1017/CBO9781107706910.

[4] Matthias Blau and Stefan Theisen. "String theory as a theory of quantum gravity: A status report". In: *Gen. Rel. Grav.* 41 (2009), pp. 743–755. DOI: 10.1007/s10714-008-0752-z.

[5] Luca Bombelli et al. "Space-time as a causal set". In: *Phys. Rev. Lett.* 59 (5 Aug. 1987), pp. 521–524. DOI: 10.1103/PhysRevLett.59.521.

[6] S. W. Hawking, A. R. King, and P. J. McCarthy. "A new topology for curved space–time which incorporates the causal, differential, and conformal structures". In: *Journal of Mathematical Physics* 17.2 (1976), pp. 174–181. DOI: 10.1063/1.522874.

[7] David B. Malament. "The class of continuous timelike curves determines the topology of spacetime". In: *Journal of Mathematical Physics* 18.7 (1977), pp. 1399–1404. DOI: 10.1063/1.523436.

[8] Onkar Parrikar and Sumati Surya. "Causal topology in future and past distinguishing spacetimes". In: *Classical and Quantum Gravity* 28.15 (July 2011), p. 155020. DOI: 10.1088/0264-9381/28/15/155020.

[9] Fay Dowker. "Introduction to causal sets and their phenomenology". In: *Gen. Rel. Grav.* 45.9 (2013), pp. 1651–1667. DOI: 10.1007/s10714-013-1569-y.

[10] E. Minguzzi and M. Sanchez. "The causal hierarchy of spacetimes". 2006. DOI: 10.48550/ARXIV.GR-QC/0609119.

[11] Rafael D. Sorkin. "1983 paper on entanglement entropy: "On the Entropy of the Vacuum outside a Horizon"". In: *10th International Conference on General Relativity and Gravitation*. Vol. 2. 1984, pp. 734–736. arXiv: 1402.3589 [gr-qc].

[12] Luca Bombelli et al. "Quantum source of entropy for black holes". In: *Phys. Rev. D* 34 (2 July 1986), pp. 373–383. DOI: 10.1103/PhysRevD.34.373.

[13] Joe Henson. "The causal set approach to quantum gravity". 2006. DOI: 10.48550/ARXIV.GR-QC/0601121.

[14] Mehdi Saravani and Siavash Aslanbeigi. "On the causal set–continuum correspondence". In: *Classical and Quantum Gravity* 31.20 (Oct. 2014), p. 205013. DOI: 10.1088/0264-9381/31/20/205013.

[15] Luca Bombelli, Joe Henson, and Rafael D. Sorkin. "DISCRETENESS WITHOUT SYMMETRY BREAKING: A THEOREM". In: *Modern Physics Letters A* 24.32 (Oct. 2009), pp. 2579–2587. DOI: 10.1142/S0217732309031958.

[16] Fay Dowker and Jeremy Butterfield. "Recovering General Relativity from a Planck scale discrete theory of quantum gravity". 2021. DOI: 10.48550/ARXIV.2106.01297.

[17] David A. Meyer. "The dimension of causal sets". PhD thesis. Massachusetts Institute of Technology, 1989. eprint: http://hdl.handle.net/1721.1/14328.

[18] Mriganko Roy, Debdeep Sinha, and Sumati Surya. "Discrete geometry of a small causal diamond". In: *Phys. Rev. D* 87 (4 Feb. 2013), p. 044046. DOI: 10.1103/PhysRevD.87.044046.

[19] Seth Major, David Rideout, and Sumati Surya. "On recovering continuum topology from a causal set". In: *Journal of Mathematical Physics* 48.3 (2007), p. 032501. DOI: 10.1063/1.2435599.

[20] Graham Brightwell and Ruth Gregory. "Structure of random discrete spacetime". In: *Phys. Rev. Lett.* 66 (3 Jan. 1991), pp. 260–263. DOI: 10.1103/PhysRevLett.66.260.

[21] Astrid Eichhorn, Sumati Surya, and Fleur Versteegen. "Induced spatial geometry from causal structure". In: *Classical and Quantum Gravity* 36.10 (Apr. 2019), p. 105005. DOI: 10.1088/1361-6382/ab114b.

[22] Dionigi M. T. Benincasa and Fay Dowker. "Scalar Curvature of a Causal Set". In: *Phys. Rev. Lett.* 104 (18 May 2010), p. 181301. DOI: 10.1103/PhysRevLett.104.181301.

[23] D. J. Kleitman and B. L. Rothschild. "Asymptotic enumeration of partial orders on a finite set". In: *Trans. Amer. Math. Soc.* 205 (1975), pp. 205–220. DOI: 10.1090/S0002-9947-1975-0369090-9.

[24] Dionigi Maria Teofilo Benincasa. "The action of a casual set". PhD thesis. Imperial College London, 2013. DOI: https://doi.org/10.25560/14170.

[25] S P Loomis and S Carlip. "Suppression of non-manifold-like sets in the causal set path integral". In: *Classical and Quantum Gravity* 35.2 (Dec. 2017), p. 024002. DOI: 10.1088/1361-6382/aa980b.

[26] Sumati Surya. "Evidence for the continuum in 2D causal set quantum gravity". In: *Classical and Quantum Gravity* 29.13 (June 2012), p. 132001. DOI: 10.1088/0264-9381/29/13/132001.

[27] Lisa Glaser. "The Ising model coupled to 2d orders". In: *Classical and Quantum Gravity* 35.8 (Mar. 2018), p. 084001. DOI: 10.1088/1361-6382/aab139.

[28] Lisa Glaser and Sumati Surya. "The Hartle–Hawking wave function in 2D causal set quantum gravity". In: *Classical and Quantum Gravity* 33.6 (Feb. 2016), p. 065003. DOI: 10.1088/0264-9381/33/6/065003.

[29] D. P. Rideout and R. D. Sorkin. "Classical sequential growth dynamics for causal sets". In: *Phys. Rev. D* 61 (2 Dec. 1999), p. 024002. DOI: 10.1103/PhysRevD.61.024002.

[30] Xavier Martin et al. ""Renormalization" transformations induced by cycles of expansion and contraction in causal set cosmology". In: *Physical Review D* 63.8 (Mar. 2001). DOI: 10.1103/physrevd.63.084026.

[31] Rafael D. Sorkin. "QUANTUM MECHANICS AS QUANTUM MEASURE THEORY". In: *Modern Physics Letters A* 09.33 (1994), pp. 3119–3127. DOI: 10.1142/S021773239400294X.

[32] Fay Dowker, Steven Johnston, and Sumati Surya. "On extending the quantum measure". In: *Journal of Physics A: Mathematical and Theoretical* 43.50 (Nov. 2010), p. 505305. DOI: 10.1088/1751-8113/43/50/505305.

[33] Sumati Surya. "The causal set approach to quantum gravity". In: *Living Reviews in Relativity* 22.1 (Sept. 2019). ISSN: 1433-8351. DOI: 10.1007/s41114-019-0023-1.

[34] Astrid Eichhorn. "Steps towards Lorentzian quantum gravity with causal sets". In: *Journal of Physics: Conference Series* 1275 (Sept. 2019), p. 012010. DOI: 10.1088/1742-6596/1275/1/012010.

[35] Jan Ambjorn et al. "Renormalization in Quantum Theories of Geometry". In: *Frontiers in Physics* 8 (2020). ISSN: 2296-424X. DOI: 10.3389/fphy.2020.00247.

[36] R Loll. "Quantum gravity from causal dynamical triangulations: a review". In: *Classical and Quantum Gravity* 37.1 (Dec. 2019), p. 013002. DOI: 10.1088/1361-6382/ab57c7.

[37] Astrid Eichhorn. "Towards coarse graining of discrete Lorentzian quantum gravity". In: *Classical and Quantum Gravity* 35.4 (Jan. 2018), p. 044001. DOI: 10.1088/1361-6382/aaa0a3.

[38] Alessandro Codello, Roberto Percacci, and Christoph Rahmede. "Investigating the ultraviolet properties of gravity with a Wilsonian renormalization group equation". In: *Annals of Physics* 324.2 (Feb. 2009), pp. 414–469. DOI: 10.1016/j.aop.2008.08.008.

[39] Dario Benedetti, Pedro F. Machado, and Frank Saueressig. "Asymptotic Safety in Higher-Derivative Gravity". In: *Modern Physics Letters A* 24.28 (Sept. 2009), pp. 2233–2241. DOI: 10.1142/s0217732309031521.

[40] Aleksandr Kurov and Frank Saueressig. "On Characterizing the Quantum Geometry Underlying Asymptotic Safety". In: *Frontiers in Physics* 8 (2020). ISSN: 2296-424X. DOI: 10.3389/fphy.2020.00187.

[41] R. D. Sorkin. "Does locality fail at intermediate length scales?" In: *Approaches to Quantum Gravity: Toward a New Understanding of Space, Time and Matter*. Ed. by DanieleEditor Oriti. Cambridge University Press, 2009, pp. 26–43. DOI: 10.1017/CBO9780511575549.004.

[42] Alessio Belenchia, Dionigi M T Benincasa, and Fay Dowker. "The continuum limit of a 4-dimensional causal set scalar d'Alembertian". In: *Classical and Quantum Gravity* 33.24 (Dec. 2016), p. 245018. ISSN: 1361-6382. DOI: 10.1088/0264-9381/33/24/245018.

[43] Fay Dowker and Lisa Glaser. "Causal set d'Alembertians for various dimensions". In: *Classical and Quantum Gravity* 30.19 (Sept. 2013), p. 195016. ISSN: 1361-6382. DOI: 10.1088/0264-9381/30/19/195016.

[44] Lisa Glaser. "A closed form expression for the causal set d'Alembertian". In: *Classical and Quantum Gravity* 31.9 (Apr. 2014), p. 095007. ISSN: 1361-6382. DOI: 10.1088/0264-9381/31/9/095007.

[45] Leo Brewin. "Riemann normal coordinates, smooth lattices and numerical relativity". In: *Classical and Quantum Gravity* 15.10 (Oct. 1998), pp. 3085–3120. ISSN: 1361-6382. DOI: 10.1088/0264-9381/15/10/014.

[46] Helmut Friedrich, István Rácz, and Robert M. Wald. "On the Rigidity Theorem for Spacetimes with a Stationary Event Horizon or a Compact Cauchy Horizon". In: *Communications in Mathematical Physics* 204.3 (Aug. 1999), pp. 691–707. ISSN: 1432-0916. DOI: 10.1007/s002200050662.

[47] Surbhi Khetrapal and Sumati Surya. "Boundary term contribution to the volume of a small causal diamond". In: *Classical and Quantum Gravity* 30.6 (Feb. 2013), p. 065005. ISSN: 1361-6382. DOI: 10.1088/0264-9381/30/6/065005.

[48] Matthias Blau, Denis Frank, and Sebastian Weiss. "Fermi coordinates and Penrose limits". In: *Classical and Quantum Gravity* 23.11 (May 2006), pp. 3993–4010. ISSN: 1361-6382. DOI: 10.1088/0264-9381/23/11/020.

[49] Wolfram Research Inc. *Generalized hypergeometric function 2F2: Representations through more general functions (formula 07.25.26.0004)*. 2001. URL: http://functions.wolfram.com/07.25.26.0004.01 (visited on 04/26/2022).

[50] Wolfram Research Inc. *Meijer G-function: Specific values (formula 07.34.03.0032)*. 2001. URL: http://functions.wolfram.com/07.34.03.0032.01 (visited on 04/26/2022).

[51] Wolfram Research Inc. *Generalized hypergeometric function: Specific values (formula 07.31.03.0008)*. 2001. URL: http://functions.wolfram.com/07.31.03.0008.01 (visited on 04/26/2022).

[52] Wolfram Research Inc. *Generalized incomplete gamma function: Representations through more general functions (formula 06.07.26.0002)*. 2001. URL: http://functions.wolfram.com/06.07.26.0002.01 (visited on 04/26/2022).

[53] Will Cunningham. *CausalSetGenerator*. 2017. URL: https://bitbucket.org/dk-lab/causalsetgenerator/src/master/ (visited on 05/06/2022).

[54] Lisa Glaser. *IsingCauset*. URL: https://github.com/LisaGlaser/IsingCauset (visited on 05/06/2022).

[55] Christopher Pfeiffer. *CausalSetCurvature*. 2022. URL: https://github.com/cdPfeiffer/CausalSetCurvature.